Acta Materialia 319 (2026) 122665

Contents lists available at ScienceDirect

Acta Materialia

journal homepage: www.elsevier.com/locate/actamat

Full length article

Solid oxide cells degradation by Nickel oxidation: A phase field study of oxide growth and its mechanical impact

Sylvain Fournier [a,*], Maxime Hubert [a], Kassem Dia [b], Thomas David [b], Aurélien Doitrand [c], Gergely Molnár [d], Sylvain Meille [c], Jérôme Laurencin [a]

[a] Univ. Grenoble Alpes, CEA, Liten, DTCH, 38000, Grenoble, France
[b] Univ. Grenoble Alpes, CEA, Liten, DTNM, 38000, Grenoble, France
[c] Univ Lyon, INSA Lyon, Universite Claude Bernard Lyon 1, CNRS, MATEIS, UMR5510, 69621, Villeurbanne, France
[d] CNRS, INSA Lyon, LaMCoS, UMR5259, 69621, Villeurbanne, France

ARTICLE INFO

Keywords:
Phase field modeling
Oxidation
Nickel
Solid oxide cells
Composite

ABSTRACT

Solid Oxide Cells are highly efficient energy conversion devices that can be damaged by various system failures. Specifically, the porous hydrogen electrode, which is a cermet consisting of Nickel and Yttria Stabilized Zirconia (Ni-YSZ), can deteriorate when exposed to oxidizing atmosphere at high temperature. Ni oxidation induces volumetric expansion which is partially accommodated in the pores of the cermet. This constrained swelling imposes mechanical strain on the YSZ backbone that can compromise its integrity. In this study, a conventional cermet was oxidized in air at 700 °C for different times to characterize the kinetics and features of Ni oxidation and the fracture of YSZ. A novel three-material phase field model, incorporating oxidation-induced strains, was developed to simulate Ni oxidation within the complex electrode microstructure. The model was validated on different cermet microstructures to reproduce the kinetics of oxidation in the different electrode layers and the YSZ mechanical loading after oxidation. The material parameters governing oxidation (Ni diffusion in NiO) and stress state (oxide growth strain) were identified through the model calibration. A correlation between oxidation and microstructural features was identified, revealing that Ni coarsening slows oxidation kinetics, and enabling DoO estimation prior to simulation with a microstructure descriptor. Simulations revealed localized high tensile stresses at several YSZ necks, matching experimental crack initiation timescales and validating a first step towards oxidation-induced damage prediction.

1. Introduction

Porous materials play a critical role in a wide range of cutting-edge technologies. For instance, they allow maximizing heat exchange in ceramic or metallic foams [1], enhancing catalytic surface area in fuel reforming or in Solid Oxide Cells (SOCs) [2,3], enabling fluid transport in membrane filters [4,5], and reducing the structural weight of aeronautical and spatial components [6]. In these applications, they are usually exposed to severe operating conditions at high temperatures under oxidizing environments. These conditions can induce a significant risk of oxidation in the porous material, which can compromise both its functional properties and structural integrity [7–10].

SOCs are a particularly relevant example of these challenges. The hydrogen electrode of standard SOCs is a porous cermet made of Nickel and Yttria Stabilized Zirconia (Ni-YSZ). This porous composite electrode ensures efficient gas diffusion and provides numerous reactive sites at Triple Phase Boundary (TPB) lines [11]. The combination of these structural features with operation at elevated temperatures (650 °C to 850 °C) in a reducing environment makes the hydrogen electrode particularly vulnerable to various failure modes that can cause detrimental Ni oxidation. This Ni oxidation is sometimes called reoxidation since the cermet is manufactured using Nickel Oxide (NiO) particles prior to reduction which makes it operational. Potential sources of oxygen exposure include a gas leak during operation, fuel overutilization in fuel cell mode, and unexpected air reintroduction during system shutdown [12]. At high temperatures, the exposition of metallic Ni to an oxidizing atmosphere induces its oxidation which involves a significant volumetric expansion [13–15]. The subsequent nickel oxide growth during oxidation progressively fills the cermet porosity and also applies deformation to the YSZ backbone. This deformation generates tensile stress in the ceramic component that can induce its local microcracking [16]. Full oxidation of the cermet and redox cycling have been shown to deteriorate cell performances and may even provoke

* Corresponding author.
E-mail address: fourniersylvain@protonmail.com (S. Fournier).

https://doi.org/10.1016/j.actamat.2026.122665
Received 16 January 2026; Received in revised form 12 August 2026; Accepted 12 August 2026
Available online 19 August 2026

catastrophic failure of the YSZ electrolyte [17–20]. While the effects of complete oxidation are well documented, it appears essential to better understand the influence of partial oxidation on the onset and evolution of micro-damage in SOCs. Moreover, the role of the electrode microstructure on the Ni oxidation kinetic and stresses in the YSZ is still unclear.

The mechanism of NiO growth at high temperature has been widely studied and described in the literature, particularly for flat and dense Ni thin films [15,21–25]. For films thicker than 20 nm, the oxidation behavior is generally well described by Wagner's theory, which predicts parabolic growth kinetics, governed by a diffusion-limited mechanism [26–28]. Atkinson [28] and later studies [29] have demonstrated that Ni^{2+} diffusion through the NiO layer is several orders of magnitude faster than O^{2-} diffusion. The kinetics of Ni oxidation is thus controlled by the diffusion of Ni^{2+} cations towards the oxide/gas interface. Using tracer diffusion of Ni in the NiO lattice [28], it has been observed that grain boundary diffusion is the dominant pathway for Ni^{2+} transport between 500 and 800 °C, accelerating the kinetics compared to bulk diffusion. Indeed, it has been found that the formation energy of cation vacancies is lower at grain boundaries than in the bulk of the NiO crystal grains [22].

The diffusion of Ni^{2+} towards the oxide/gas interface during the oxidation process creates a residual vacancy in the metal at the metal/oxide interface. The accumulation of these vacancies in the vicinity of the interface adds an additional strain into the materials. However, the vacancies are also likely to migrate into the Ni metal phase, or be annihilated by dislocation slip [30]. When Ni vacancies migration dominates [25], they can diffuse and coalesce to form nanopores into the bulk of the metal particles, as it has sometimes been observed experimentally for SOCs [16,31]. When vacancies annihilation governs, interfacial dislocations climb and glide [32–35], enabling the displacement of the metal-oxide interface without damage [28,36]. When strain accumulation overcomes relaxation mechanisms such as dislocation motion, the oxide or its interface with the metal is damaged, including decohesion, buckling, spalling, cracking and/or the formation of voids directly at the Ni/NiO interface [37–40]. A combination of these phenomena can lead to duplex film growth or successive film spalling and reformation [24,37], although the structure of connected Ni particles in SOCs tends to mitigate this behavior [31]. Overall, these mechanisms lead to the inward motion of the metal/oxide interface in addition to the outward growth of the oxide/gas interface.

Studies of high-temperature oxidation of Ni plates have shown that the resulting oxide is generally porous, with grains elongated along the growth direction, although its morphology can vary with oxidation temperature and time [41]. In this geometry, the growth of intergranular oxide is considered as the major source of stress in the NiO layer due to the fast oxygen and nickel ions diffusion along grain boundaries according to Rhines theory and subsequent studies [32,42–44]. This mechanism is supported by experimental observations of lateral oxide growth and local thickening at grain boundaries [43,45]. These growth stresses can also induce the cracking of the NiO scale [14], creating additional diffusion paths for gaseous oxygen and new oxide growth sites inside the oxide layer. In SOCs, the irregular Ni phase topology promotes rough and sponge-like NiO layers made of platelets [35,46,47], a topology that is linked to the development of mechanical stresses within the oxide layer.

In the complex microstructure of a cermet used in SOCs, the local deformation applied on the YSZ backbone during oxidation can have several origins. While the exact cause is unclear, it may be due to lateral oxide growth and particle swelling. These expansions generate tensile stresses in YSZ that can lead to microcracking, as exemplified by Nakajo et al. [18], who reported microcracks in YSZ after full Ni oxidation. Other studies have observed that multiple redox cycles induce microcracking in YSZ and have correlated this with degradation of cell performance [20,48]. Few studies tried to capture progressive oxidation at intermediate stages [49], although it provides more insight on the onset of hydrogen electrode degradation mechanisms.

As the mechanisms of nickel oxidation coupled with stress build-up in solid phases are complex and closely linked to the cermet microstructure, modeling appears to be a relevant approach for understanding all the involved phenomena. In this context, the phase field method (PFM) [50–52] is increasingly used as a diffuse-interface approach to describe the phase evolution during high temperature oxidation [27,53,54]. This method is especially relevant to model oxidation of metals in air, generally assuming the growth of a homogeneous oxide film. In the literature, most of the studies described the evolution of one interface in biphasic systems: the metal-oxide phases for the inward growth of the interface as proposed for the oxidation of zirconium or aluminum [27,54–56], and the oxide-gas phases for the outward growth of the interface as developed for the nickel oxidation [57]. Despite its capital importance to simulate the Ni oxidation, the implementation of triphasic systems involving metal/oxide/gas phases is more complex. Zaeem et al. [58] and Johnson [59] have investigated this kind of model but implemented it on restricted one-dimensional geometries. Both biphasic or triphasic phase field models have generally been applied to simple geometries, the most complex cases would use simple rectangular domains with roughened surfaces [27,54,55,57]. Regarding the SOC application, the complexity of cermet microstructure cannot be ignored as it plays a crucial role in the Ni oxidation. However, to the best of our knowledge, no PFM model has been proposed to simulate Ni oxidation in the electrode. Only Jiao et al. [60] have developed a PFM model to simulate the reduction of NiO into Ni in these complex microstructures. Moreover, the impact of nickel oxidation on YSZ stress state and subsequent crack formation has been investigated using purely mechanical PFMs in a few studies [61–63]. These models typically approximate the oxidation-induced swelling by a simple expansion of the Ni phase to compute the stresses in YSZ. Nevertheless, such approaches do not explicitly model the Ni oxidation process itself, nor the resulting phase evolution in the microstructure and the oxidation strain.

In this work, a phase field model is proposed to simulate the Ni oxidation in the typical cermet microstructure of SOCs. Specifically, the aim of this work is to capture the coupled evolution of the Ni/NiO and NiO/gas interfaces during oxidation by explicitly describing the metal, oxide, and pore phases. In addition to the phase evolutions, the mechanical energy contribution is also included in the PFM in order to simulate the stresses in the solid phases including the YSZ backbone. The calibration of the parameters in the PFM is done using experimental data on kinetics of oxidation in a conventional SOC cermet. In particular, characterization of the cermet microstructure after different time of exposition to air allows to retrieve the evolution of degree of Ni oxidation as a function of time. Finally, the validated model is used to assess the influence of microstructural features and material properties on oxidation and stress development in such structures.

2. Materials and methods

In this section, a description of the cell used for the oxidation experiments is proposed as well as details about the analysis of the electrode microstructure and the determination of the oxidation degree.

2.1. Materials

A hydrogen electrode made of two layers has been used for the study of oxidation. The H_2 electrode is composed of a thick support layer of about 280 µm, which is a cermet of nickel and 3 mol.% Yttria stabilized zirconia (Ni – 3 YSZ). The second part of the electrode is a functional layer of about 25 µm made of Ni – 8 YSZ. All the details about the hydrogen electrode microstructure have already been published in a previous article [64]. The phase volume fractions of the reduced initial cell used here are typically about 38.0 vol.% of Ni; 36.7 vol.% of YSZ;

25.3 vol.% of porosity in the functional layer and of 28.8 vol.% of Ni; 40.1 vol.% for YSZ; 31.0 vol.% of porosity in the support layer. It should be noted that the hydrogen electrode samples are manufactured from YSZ and NiO powders, resulting in NiO-YSZ composites that are later reduced to obtain Ni-YSZ operational electrodes. The functional layer is fully dense in its oxidized state and the porosity is only induced by the reduction of NiO into Ni. On the contrary, pores are already present in the NiO-3YSZ support before reduction.

2.2. Experimental methods

To obtain the initial operable electrode microstructure made of Ni-YSZ, the first step is to fully reduce the NiO into its metallic phase. For this purpose, the electrode was exposed to a mixture of hydrogen and argon (2 %H_2/Ar) during 48 hours at 800 °C. The heating and cooling were performed at a constant rate of 1 °C.min^{-1}. This reduction process induces the formation of porosity within the electrode due to the volumetric contraction of NiO upon reduction. Afterwards, the electrode bilayer was cut into several individual samples. Each of them was subjected to an oxidation process (usually called reoxidation since the cell is originally NiO-YSZ). The oxidation protocol started with heating the sample up to 700 °C at a rate of 1 °C.min^{-1} in Ar atmosphere. Then, the sample was exposed to air at 700 °C for a specific duration $t \in \{0; 2; 5; 10; 20; 30; 120\}$ min, and cooled down in the same conditions as for heating. It can be noted that a high airflow rate was supplied to the sample to ensure that oxidation was not limited by oxygen feeding, but fully controlled by the kinetics of the Ni/NiO transition.

The samples were weighed at each step of the protocol (before reduction, after reduction and after oxidation). The mass measurements were carried out on a balance with a precision of 0.1 mg. The precise weighting of the samples enables verification of the initial reduction of the nickel phase and afterwards to estimate the oxidation degree. The degree of oxidation (DoO) of nickel is then calculated as follows [49]:

$$DoO(t) = \frac{m(t) - m(t=0)}{m(DoO = 100\%) - m(t=0)} \tag{1}$$

with $m(t)$ the mass of the sample after exposition to air, $m(t=0)$ the mass of the same sample after reduction protocol, and $m(DoO = 100\%)$ its mass in the fully oxidized state. As the thick support layer accounts for most of the mass of the hydrogen electrode, it is difficult to assess the oxidation state of the thin functional layer using this method. To overcome this issue, cross-sectional analyses of the samples were carried out using scanning electron microscopy (SEM). The samples were embedded in epoxy resin, polished and coated with a 5 nm carbon layer to avoid charging during imaging. SEM imaging and energy-dispersive X-ray spectroscopy (EDS) mapping were conducted using a Zeiss Gemini SEM 460 equipped with an Oxford Ultim Max 100 EDS detector. The voltage was set at 1.1 kV for imaging, while EDS maps were acquired at 10 kV. Images including both the functional layer and the support layer were obtained with a pixel size of 22.3 nm and a dimension of about 92 µm × 63 µm. To overcome interruptions caused by vibration or drift during prolonged acquisition times, the EDS maps were acquired at half the resolution of the corresponding SEM images. After acquisition, the EDS maps were upsampled and precisely aligned with the SEM images with a custom python script using skimage library [65]. In order to retrieve the relative amount of the different phases in the SEM images (Ni, NiO, YSZ, pores), a U-Net convolutional neural network was used. This algorithm has been trained in a supervised fashion on similar images using cross-entropy loss to learn the mapping between SEM textures and material phases. The details of the deep learning-based methodology can be found in [66]. As an example, the SEM image of the sample oxidized for 2 h and its segmented version are displayed in supplementary material section S-1. After image segmentation of the different samples, it is possible to estimate the DoO for both the functional and support layers from the volume fraction of Ni and NiO phases. To this end, Eq. (1) was adapted to the segmented images data:

$$DoO(t) = \frac{m_{\mathrm{Ni}}(t) + m_{\mathrm{NiO}}(t) - (m_{\mathrm{Ni}}(t) + d_{\mathrm{NiO-Ni}} m_{\mathrm{NiO}}(t))}{d_{\mathrm{Ni-NiO}} m_{\mathrm{Ni}}(t) + m_{\mathrm{NiO}}(t) - (m_{\mathrm{Ni}}(t) + d_{\mathrm{NiO-Ni}} m_{\mathrm{NiO}}(t))} \tag{2}$$

In this equation, m_{Ni} and m_{NiO} were obtained by multiplying the surface area of the Ni and NiO phases observed in the 2D SEM images with their respective density. The factor $d_{\mathrm{NiO-Ni}}$ (resp. $d_{\mathrm{Ni-NiO}}$) is used to convert the mass of NiO into the corresponding mass of Ni (resp. mass of Ni into mass of NiO) and is expressed as:

$$d_{\mathrm{NiO-Ni}} = \frac{V_{\mathrm{m}}^{\mathrm{NiO}}}{V_{\mathrm{m}}^{\mathrm{Ni}}} \frac{\rho_{\mathrm{O}}}{\rho_{\mathrm{M}}} \tag{3}$$

with $V_{\mathrm{m}}^{\mathrm{NiO}}$ and $V_{\mathrm{m}}^{\mathrm{Ni}}$ the molar volumes of oxide and metal phases, and ρ_{O} and ρ_{M} their respective densities. The ratio between the molar volumes allows applying a swelling to the volume fraction of Ni to reproduce the space taken if this metallic Ni was fully oxidized. The ratio of density is used to obtain the mass of this equivalent oxide phase. The Eq. (2) has the advantage of being applicable to experimental segmented images and to simulation results without relying on the measurement of reference samples to obtain the initial mass in the reduced and fully oxidized states ($m(t=0)$ and $m(DoO = 100\%)$). Thus, the degree of oxidation can be determined separately for the functional and support layers.

3. Model description

3.1. Phase field formulation

The phase field method is used to describe the microstructural evolution during phase transformation. The basic idea is to represent the phases using a so-called phase field variable, ϕ which remains constant within phases and exhibits steep but smooth evolution at interfaces (known as diffuse interfaces). This method has become increasingly popular in the recent years due to its simplicity and flexibility.

For the current work, the phase field model must reproduce the evolution of the oxide phase in between the metal and the pores, as well as the stresses induced in the YSZ backbone. The oxidation model is applied to the Ni, NiO, and pore phases, respectively abbreviated M for metal, O for oxide and P for pore as depicted in Fig. 1. This model follows the framework of standard oxidation phase field models, with the work of Ammar et al. [55] serving as a key reference. It involves one conserved variable c and a non-conserved variable ϕ, each defined in a two-dimensional cartesian space (x, y) and evolving with time t. The variable c represents the molar fraction of diffusible nickel (Ni), which means the Ni that can diffuse between the different phases. It is expressed as $c = \frac{c_{\mathrm{Ni}}}{c_{\mathrm{Ni}}^{max}}$ with $c_{\mathrm{Ni}}^{max} = c_{\mathrm{Ni}}^{M}$ the stable concentration of Ni in the nickel phase. The variable ϕ is the order parameter, which is defined as $\phi = \frac{c_{\mathrm{NiO}}}{c_{\mathrm{NiO}}^{max}}$, such that $\phi = 1$ in the NiO phase and $\phi = 0$ in the Ni and pore phases (with a smooth transition at the interfaces).

The present model assumes the pre-existence of a continuous thin NiO layer along the Ni interfaces prior to simulation. This assumption relies on experimental SEM observations showing a thin NiO scale surrounding Ni particles from the earliest experimental measurement time. Consequently, the model is formulated specifically to simulate outward diffusion-controlled oxide growth, and mechanical stress evolution that drives YSZ cracking in complex cermet microstructures. It describes cases of oxidation in transient conditions where oxygen partial pressure is high enough to not be the limiting mechanism. It should be noticed that the present implementation does not aim at capturing oxide nucleation on metal–pore interfaces. Moreover, the model cannot be used to describe the electrochemical reoxidation of a cermet in the case of fuel starvation [67] or the formation of NiO at the Ni/YSZ interface under operation [68].

Knowing that ϕ has the same value in the Ni and pore phases, the identification of the Ni, NiO, pore and YSZ phases is challenging

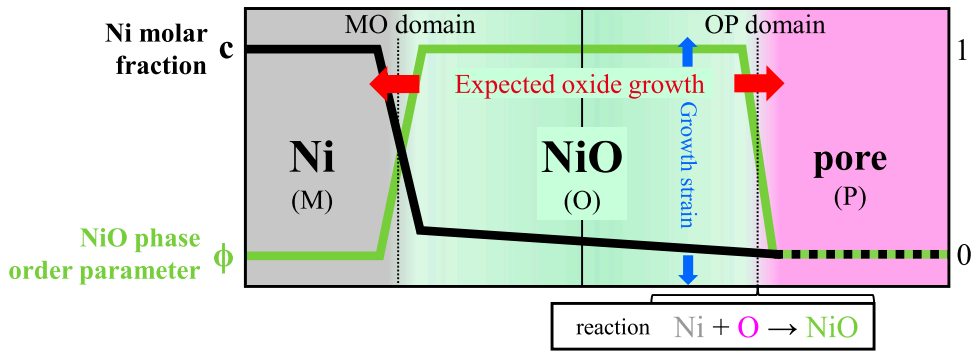

Fig. 1. Schematic representation of the oxidation model describing the two domains (MO and OP), the three considered phases (Ni=M, NiO=O and pore = P), the values of the phase field order parameter ϕ, the diffusible nickel molar fraction c, and the oxidation reaction.

in the complex electrode microstructure. To overcome this issue, we propose to divide the initial geometry into three domains: MO which can contain M and O phases; OP which can contain O and P; and YSZ which is excluded from the oxidation model but takes part in the mechanical interactions of the system (Fig. 1). The boundary between MO and OP domains corresponds to the interface between Ni and the pore phase before the oxidation (*i.e.*, microstructure in the reduced state). The thin layer of NiO considered to initiate the simulation is thus applied along this interface over about 100 nm. The MO, OP and YSZ domains remain fixed during the simulation. MO and OP are identified by integer indicators i_{MO} and i_{OP}, which are equal to one when in their respective domain and zero elsewhere (*i.e.*, $i_{\mathrm{MO}} = 1$ in the MO domain and $i_{\mathrm{OP}} = 1$ in the OP domain as shown in Fig. 1). These indicators are used to ascribe the correct material properties or governing equations in each phase. Indeed, combining the order parameter value i_{MO} and i_{OP}, the phase can be easily identified. The metallic phase M is defined by $\phi = 0 \cap i_{\mathrm{MO}} = 1$, the pore phase P by $\phi = 0 \cap i_{\mathrm{OP}} = 1$, and the oxide phase O by $\phi = 1 \cap (i_{\mathrm{MO}} = 1 \cup i_{\mathrm{OP}} = 1)$.

3.2. Functional

The evolution of the system is governed by chemical, interfacial and mechanical energy contributions, which together define the total Gibbs free energy of the system, as expressed in Eq. (4):

$$G(c,\phi,\varepsilon^{el}) = \int_{\mathrm{V}} \left[f^{Ni}_{\mathrm{chem}}(c(\boldsymbol{r},t),\phi(\boldsymbol{r},t)) + f^{\phi}_{\mathrm{interface}}(\phi(\boldsymbol{r},t)) + f_{\mathrm{mecha}}(\varepsilon^{el}(\boldsymbol{r},t),\phi(\boldsymbol{r},t)) \right] \mathrm{d}V \tag{4}$$

with t and $\boldsymbol{r}$ respectively denoting the time and the position vector. The term $f^{Ni}_{\mathrm{chem}}(c,\phi)$ is the chemical energy which penalizes deviations from the molar fraction at equilibrium in each phase. The term $f^{\phi}_{\mathrm{interface}}(\phi)$ is related to the contribution of the interfaces. It contains the energy barrier described by a double-well potential separating two phases and a gradient term that tends to minimize the length of the interfaces: $f^{\phi}_{\mathrm{interface}}(\phi) = f^{\phi}_{\mathrm{double-well}}(\phi) + f_{\mathrm{grad}}(\phi)$. The term $f_{\mathrm{mecha}}(\varepsilon^{el},\phi)$ is the mechanical energy contribution.

The chemical free energy density is expressed with the contribution of each phase as shown in the following equation:

$$f^{\mathrm{Ni}}_{\mathrm{chem}}(c,\phi) = \frac{1}{2}\left[i_{\mathrm{MO}}(1-p(\phi))k_{\mathrm{M}}\left(c-c_{\mathrm{M}}\right)^2 + p(\phi)k_{\mathrm{O}}\left(c-c_{\mathrm{O}}\right)^2 + i_{\mathrm{OP}}(1-p(\phi))k_{\mathrm{P}}\left(c-c_{\mathrm{P}}\right)^2 \right] \tag{5}$$

This last expression involves the curvature k_{A} of each square function $(c-c_{\mathrm{A}})^2$ which are calibrated to simulate accurately the experimental results. The molar fractions at equilibrium c_{A} are defined as the ratio between the equilibrium concentration of Ni c^{A}_{Ni} in phase A for $A \in \{M;O;P\}$ and the maximal Ni concentration c^{max}_{Ni}, taken equal to the equilibrium concentration in the metal phase c^{M}_{Ni}:

$$c_{\mathrm{M}} = \frac{c^{M}_{\mathrm{Ni}}}{c^{max}_{\mathrm{Ni}}}, c_{\mathrm{O}} = \frac{c^{O}_{\mathrm{Ni}}}{c^{max}_{\mathrm{Ni}}} \text{ and } c_{\mathrm{P}} = \frac{c^{P}_{\mathrm{Ni}}}{c^{max}_{\mathrm{Ni}}}. \tag{6}$$

The equilibrium concentration of Ni in the metal and the pore domains is taken from Lin et al.'s study [57] setting $c^{M}_{\mathrm{Ni}} = 152\,439\,\mathrm{mol.m^{-3}}$ and $c^{P}_{\mathrm{Ni}} = 0\,\mathrm{mol.m^{-3}}$, while we set $c^{O}_{\mathrm{Ni}} = 815\,\mathrm{mol.m^{-3}}$ (half of the saturation value given by Lin et al.) in the oxide, since their value is the maximum amount of Ni that can diffuse in NiO. Hence, the equilibrium value of variable c is $c_{\mathrm{M}} = 1$ in phase M ; $c_{\mathrm{O}} \approx 0.005$ in phase O; and $c_{\mathrm{P}} = 0$ in phase P. The values used for these parameters are reminded in Table 1. In Eq. (5), the terms i_{MO}, i_{OP} and $p(\phi)$ allow to assign contributions to each specific phase. The interpolation function $p(\phi)$ defines progressive variation of properties between phases, evolving continuously from $p(\phi=0)=0$ to $p(\phi=1)=1$. Following the study by Wang et al. [69], the interpolation function has been chosen to ensure a smooth transition:

$$p(\phi) = \phi^3(10 - 15\phi + 6\phi^2) \tag{7}$$

The double well potential for the two interfaces is expressed by Eq. (8):

$$f^{\phi}_{\mathrm{double-well}}(\phi) = (i_{\mathrm{MO}}W_{\mathrm{MO}} + i_{\mathrm{OP}}W_{\mathrm{OP}})\, g(\phi) \tag{8}$$

in which $g(\phi)$ is a double well function defined as $g(\phi) = \phi^2(1-\phi)^2$ and W_{AB} is the height of the energy barrier accounting for the free energy penalty of the interface AB. As it has been shown in [55,70], neglecting the terms coming from the other energy densities, the standard relation linking the height of the energy barrier W_{AB} with the ratio between the interfacial energy σ_{AB} and the prescribed interface thickness ζ_{AB} can be obtained with:

$$W_{\mathrm{AB}} = 6C\frac{\sigma_{\mathrm{AB}}}{\zeta_{\mathrm{AB}}}. \tag{9}$$

When taking the interface as the region verifying $0.05 < \phi < 0.95$, the parameter C is estimated to be $C = 2.94$ according to [70]. This relation was used to estimate values of W_{MO} and W_{OP} for the simulations (see Table 1).

The gradient term of the interfacial energy is written as:

$$f_{\mathrm{grad}}(\phi) = \frac{i_{\mathrm{MO}}\kappa_{\mathrm{MO}} + i_{\mathrm{OP}}\kappa_{\mathrm{OP}}}{2}|\nabla\phi|^2 \tag{10}$$

in which κ_{AB} is the coefficient of the gradient term of the interface AB. As for the height of the energy barrier, this parameter is also related to an interface thickness and the interface energy, when neglecting the other contributions, as explained by [70]:

$$\kappa_{\mathrm{AB}} = \frac{3}{C}\zeta_{\mathrm{AB}}\sigma_{\mathrm{AB}}. \tag{11}$$

The Eq. (11) has been used to calibrate an initial value for the simulations, as detailed in Table 1, using interfacial energy density from the literature for MO and OP interfaces [71,72].

The elastic strain energy contribution is expressed by Eq. (12):

$$f_{\mathrm{mecha}}(\varepsilon^{el},\phi) = \frac{1}{2}\, C_{\mathrm{ijkl}}\, \varepsilon^{el}_{\mathrm{ij}}\, \varepsilon^{el}_{\mathrm{kl}} \tag{12}$$

in which ε^{el} is the elastic strain tensor and C_{ijkl} is defined as:

$$C_{ijkl} = i_{MO}\,(1-p(\phi))\,C^{M}_{ijkl} + p(\phi)\,C^{O}_{ijkl} + i_{OP}\,(1-p(\phi))\,C^{P}_{ijkl} + i_{YSZ}C^{YSZ}_{ijkl} \tag{13}$$

The expression of the stiffness matrix as a function of the domain and the interpolation function allows for a continuous evolution of the elastic coefficients across the interfaces. In the model, the materials are considered isotropic, since the Ni and YSZ particles exhibit a polycrystalline microstructure with randomly oriented grains, and the NiO is modeled as a homogeneous scale, although its actual structure is more complex (cracks, delaminations, grain orientation) [28,37] and not fully characterized here. The Lamé parameters are expressed as $\lambda = \frac{E\nu}{(1+\nu)(1-2\nu)}$ and $\mu = \frac{E}{2(1+\nu)}$. The values of Young's moduli and Poisson ratio defining Lamé parameters for each material are provided in Table 1.

3.3. Governing equations

The evolution of the system is governed by three equations, respectively describing phase change, diffusion, and mechanical equilibrium.

Allen–cahn equation: ϕ

The evolution of the order parameter $\phi(\boldsymbol{r},t)$ over time and space represents the growth of the oxide layer. It is the solution of the classical Allen–Cahn equation with an interfacial reaction term r_ϕ:

$$\dot{\phi} = -L_\phi \frac{\delta G(\phi)}{\delta \phi} - r_\phi \tag{14}$$

where L_ϕ is the mobility coefficient that scales the contribution of the Gibbs free energy derivative with respect to ϕ. The term L_ϕ is calibrated to ensure the correct motion of the two interfaces between the different phases. The derivation of $\frac{\delta G(\phi)}{\delta \phi}$ from Eq. (14) is provided in Appendix A along with the developed form of the implemented Allen–Cahn equation. The interfacial reaction term r_ϕ takes into account the kinetics of interfacial reactions in the case of Ni oxidation. In the present formulation, the term r_ϕ is introduced to couple the evolution of the phase field to the local deviation from equilibrium concentration. This reaction term needs to be considered in the model since the classical Allen–Cahn equation describes interface motion driven by free energy minimization but does not picture the oxidation at the interfaces. The reaction term r_ϕ is expressed combining Eqs. (15) and (16) and allows linking the diffusible Ni molar fraction at interfaces to their motion described by the order parameter ϕ:

$$r_\phi = r_\phi^{MO} + r_\phi^{OP} \tag{15}$$

where the interface-specific reaction terms are defined by following Eqs. (16a) and (16b).

$$r_\phi^{MO} = L_r^{MO}(c - c_{eq}^{MO})\frac{dp}{d\phi} i_{MO} \tag{16a}$$

$$r_\phi^{OP} = L_r^{OP}(c - c_{eq}^{OP})\frac{dp}{d\phi} i_{OP} \tag{16b}$$

In these expressions, the term $\frac{dp}{d\phi}$ and integers i_{MO} and i_{OP} ensure to restrict the reaction term contribution to the corresponding interfacial regions. The term $(c - c_{eq}^{AB})$ drives the reaction based on deviation from the equilibrium molar fraction c_{eq}^{AB} at each interface AB. In this way, the interface is displaced whenever the local composition deviates from equilibrium, thereby ensuring consistency between phase transformation and mass transport. In other words, the term r_ϕ is introduced to describe the NiO growth governed by species transport and interfacial reactions. This formulation is consistent with previous phase field oxidation models (Cheng et al. [73] or Lin et al. [57]). The kinetic constants L_r^{MO} and L_r^{OP} of each interfacial reaction in Eqs. (16a) and (16b) are parameters that are calibrated using the experimental data in order to reproduce the overall kinetic of oxidation.

At the Ni/NiO interface (MO), the reaction term r_ϕ^{MO} describes the interface movement induced by Ni transfer from the metal phase into the oxide as a diffusing species. As described in the introduction, there are different physical mechanisms, including dislocation glide [33–35], that can be involved in such Ni-NiO interface motion. The equilibrium molar fraction at the MO interface is set at $c_{eq}^{MO} = \frac{c_M + 6c_O}{2}$, a value slightly larger than the average of c_M and c_O, in order to ensure the model stability and that the NiO phase can only grow.

At the NiO–pore interface (OP), it is assumed that the chemical reaction of Ni oxidation occurs, given that Ni diffusion in the oxide layer is faster than oxygen diffusion [28]. This assumption is in agreement with the work of Unutulmazsoy et al. [74] who showed that the oxidation reaction time is negligible compared to the diffusion time in nickel oxide scales at high temperatures. In this framework, any Ni atom reaching the OP interface is considered to react almost instantaneously with oxygen of the pore phase to form a NiO molecule. Therefore, the equilibrium molar fraction of Ni at OP interface has been set to $c_{eq}^{OP} = c_P = 0$.

Since the equilibrium fraction of Ni in the oxide c_O is higher than c_{eq}^{OP}, the profile of c (the diffusible Ni molar fraction) in the NiO layer exhibits a downward slope from MO interface to the OP interface. This gradient promotes Ni diffusion towards the OP side. Such decreasing concentration profiles driving diffusion are also found in other oxidation phase field models. To obtain a driving gradient, Ammar et al. [55] imposed a boundary concentration above the equilibrium value, while Zaeem et al. [58] have set initial concentrations with out-of-equilibrium values in all three phases. In contrast, multiphase field formulations explicitly resolve every involved chemical species, which avoid relying on these reaction terms but at the expense of a larger set of governing equations and increased computational cost [53,75]. Given the complexity of the microstructures considered in this work and the need to reproduce the experimental oxidation at the microscale, the present formulation is preferred.

Cahn–Hilliard equation: c

In the present model, the evolution of the diffusible molar fraction of Ni $c(t,\boldsymbol{r})$ is governed by a modified Cahn–Hilliard equation with a reaction term r_c:

$$\dot{c} = \nabla \cdot \left(M_c \nabla \frac{\delta G(c,\phi)}{\delta c} \right) - r_c \tag{17}$$

The first term of the right-hand side of Eq. (17) describes the diffusion of Ni. The diffusible Ni reaching the NiO/pore reaction front is consumed by the source term r_c, which in turn produces NiO. The developed form of the implemented equation after the derivation of $\frac{\delta G}{\delta c}$ from Eq. (4) is provided in Appendix A. The Onsager coefficient M_c (also called mobility of c) depends on the phase, and is described by Eq. (18):

$$M_c = i_{MO}(1-p(\phi))\frac{D_M}{k_M} + p(\phi)\frac{D_O}{k_O} + i_{OP}(1-p(\phi))\frac{D_P}{k_P} \tag{18}$$

where D_A is the diffusion coefficient of Ni in phase A and k_A is the curvature of the free energy density of phase A used in Eq. (5).

In Eq. (17), the reaction term r_c is introduced to take into account the elemental consumption due to the oxidation reaction at the OP interface. This term is expressed as:

$$r_c = i_{OP}\,\dot{\phi}\,\frac{1}{\eta} \tag{19}$$

where η represents a swelling coefficient. From Eqs. (17) and (19), it can be seen that the reaction term r_c imposes an opposite coupling between the temporal evolution of the diffusible Ni molar fraction $\dot{c}$ and the temporal evolution of the order parameter $\dot{\phi}$ at the NiO/pore interface. Specifically, a decrease of c in the oxide layer at the interface with the gas phase results in an increase by a factor η of the oxide phase parameter ϕ. In this way, it is possible to reproduce the swelling of the NiO phase during oxidation. This swelling originates from the difference in volume between the Ni and NiO unit cells. This theoretical swelling is described by the Pilling–Bedworth ratio (PBR), defined as

the ratio of the oxide molar to the metal molar volume. Since both ϕ and c represent normalized molar fractions, setting $\eta = PBR$ in r_c ensures appropriate conversion between Ni consumption and NiO formation at the OP interface.

As a general comment, it is worth noting that the model does not intend to describe the exact complex physical processes for the inward motion of the metal/oxide interface. In the model, thanks to the reaction term r_ϕ^{MO}, the voids created at the Ni/NiO interface due to Ni outward diffusion are progressively filled by newly formed NiO. In this condition, the NiO is considered porous in the model, as observed experimentally and schematically described by Jeangros et al. [37]. Besides, the effective Ni-to-NiO volume expansion ratio is thus given by $\eta_{eff} = (A + \eta A)/A = \eta + 1$ where A is the volume of voids filled by NiO at the Ni/NiO interface. Under this assumption, the effective volume expansion factor increases from the theoretical PBR of 1.7 to 2.7. However, this value of $\eta_{eff} = 2.7$ represents an upper bound compared to the ratio taken from the simulations as it does not consider the diffusible Ni stored in NiO (so that the effective ratio will be between 1.7 and 2.7). Furthermore, the magnitude of the effective overswelling depends on the imposed initial and boundary conditions, which will be detailed in the next section. Therefore, the present formulation should be interpreted as an effective mesoscale description of oxide growth that reproduces oxidation kinetics and the experimentally observed overswelling coming from defects within the NiO layer [16].

Mechanical equilibrium

The mechanical equilibrium of the whole geometry, including domains MO, OP and YSZ, is classically expressed with Eqs. (20a) and (20b):

$$\frac{\partial \sigma_{ij}}{\partial x_j} = 0 \qquad (x_j = x, y) \tag{20a}$$

$$\sigma_{ij} = C_{ijkl}\, \varepsilon_{kl}^{el} \tag{20b}$$

where σ_{ij} is the element of the stress tensor. The elastic strain ε_{ij}^{el} used in Eqs. (12) and (20b) is given by the difference between the total and the inelastic strains:

$$\varepsilon_{ij}^{el} = \varepsilon_{ij}^{tot} - \varepsilon_{ij}^{inel}. \tag{21}$$

The total strain ε_{ij}^{tot} is expressed assuming small deformations and plane strain assumptions:

$$\varepsilon_{ij}^{tot} = \frac{1}{2}\left(\frac{\partial u_i}{\partial x_j} + \frac{\partial u_j}{\partial x_i}\right) \tag{22}$$

with u_i the element of the displacement vector.

The inelastic strain ε_{ij}^{inel} in Eq. (21) can potentially have several contributions. In the present work, viscoplastic deformation of the reduced nickel at 700 °C [14] is not explicitly modeled as it is not the major phenomenon of interest. Although the mismatch in crystal lattice parameters between the metallic and the oxide phases was assumed to participate to the movement of the MO interface in previous studies [57,58], this contribution has not been considered in the present model. Indeed, the deformation related to this mismatch is limited to the vicinity of the Ni/NiO interface and is not expected to add a substantial contribution to the global kinetic of oxidation [32]. Moreover, thermal strains are not considered here as the study focuses on isothermal oxidation. Previous works have shown that, at operating temperature, thermal stresses tend to compensate residual cooling stresses formed during cell processing [76,77]. Therefore, the present study only takes into account the inelastic strains associated with the growth of NiO film since they are the main source of stress in the YSZ backbone [14,78]. A rather simple approach is adopted here as more detailed stress analyses at the NiO grain scale proposed in the literature [32,38,44,79,80] are beyond the scope of this study. The inelastic strain is thus expressed as follows:

$$\varepsilon^{inel} = \varepsilon^{g} = \begin{pmatrix} \varepsilon_{11}^{g} & 0 & 0 \\ 0 & \varepsilon_{22}^{g} & 0 \\ 0 & 0 & 0 \end{pmatrix} = \begin{pmatrix} p(\phi) N_y \varepsilon_0^{g} & 0 & 0 \\ 0 & p(\phi) N_x \varepsilon_0^{g} & 0 \\ 0 & 0 & 0 \end{pmatrix} \tag{23}$$

where ε_0^g is the growth strain constant that must be calibrated for a correct description of this phenomenon. The terms N_x and N_y allow to define the direction of the oxide growth. The growth strain is considered orthogonal to the oxide surface in accordance with Rhines' theory, which attributes its origin to the growth of interstitial NiO grains along fast diffusion paths of the oxide film oriented in its growth direction [32,38,42,57,78]. Therefore, N_x and N_y are used to determine the direction of the normalized absolute gradient of ϕ on each point (x, y) and are updated at each time step. They are defined as follows:

$$N_x = \frac{|n_x|}{n_{norm}} \text{ and } N_y = \frac{|n_y|}{n_{norm}} \tag{24a}$$

with $n_x = \frac{\partial \phi}{\partial x}$; $n_y = \frac{\partial \phi}{\partial y}$ and $n_{norm} = \left(\left(\frac{\partial \phi}{\partial x}\right)^2 + \left(\frac{\partial \phi}{\partial y}\right)^2\right)^{1/2}$. The orientations N_x and N_y are updated at each time step, only if the condition $\phi(x, y) > 0.9$ is verified, to prevent the modification of the strain direction for an already grown oxide. Also, the N_x and N_y fields on the 2D geometry are smoothed by a geometrical filter. These steps are necessary to avoid computational instability or unrealistic gradient evaluations that can lead to numerical problems in the computation of the gradient orientation.

3.4. Implementation: Geometries, initial and boundary conditions

The chemo-mechanical model for Ni oxidation in the hydrogen electrode is implemented in the finite element software COMSOL Multiphysics. Simulations are carried out on 2D geometries selected to comply as closely as possible with the microstructural features and phase connectivity of the 3D material, as detailed below in this section. Their dimension is $10 \times 10\,\mu m^2$, which is significantly larger than the characteristic microstructural features of the functional layer microstructure used in experiments and allows capturing the main morphological behaviors at a reduced computational cost [81]. It should be noted that the same dimension is chosen for the support layer. Each geometry is partitioned into three domains: MO, OP and YSZ which respectively represent the initial Ni, pores and zirconia. Two types of geometries are considered: synthetic geometries generated using the algorithm developed by Moussaoui et al. [81], and segmented geometries obtained through the segmentation of SEM images of reduced hydrogen electrodes cross-sections. Although the Moussaoui algorithm generates 3D geometries from prescribed volume fractions and particle size distributions, representative 2D slices are selected for simulation. A specific attention is given to select the most representative slice in the 3D reconstruction for both segmented and generated geometries, by comparing the phase fractions as well as the initial Ni/pore interface distance distributions. To achieve this goal, a distance function is implemented to compute the relative distance from the MO–OP interface, for each point (x, y) in the geometry (excluding the YSZ phase), similarly to Ouyang et al.'s work [82]. In our case, the function is calculated in two different domains, taking positive values in the OP domain and negative values in the MO domain. Distance maps are computed for each 2D slice of the generated microstructures and each square sample of the segmented SEM image to select the most representative microstructure (Fig. 2a and b). The corresponding histograms are then compared to the one of a whole volume to identify the most representative 2D samples (Fig. 2c).

For all geometries, a smoothing protocol is applied to the interfaces of the domains to improve numerical stability. To achieve accurate resolution of narrow phase interfaces, the mesh consists of triangular linear elements with edge lengths on the order of 10^{-2} µm, resulting in approximately 3×10^5 elements per geometry. The element size must be small enough to describe correctly the interfaces in the phase field model. In our model, it should be noticed that the effective interface thicknesses are dependent on the chosen heights of the energy barriers and coefficients of the gradient terms, as well as the reaction term r_ϕ.

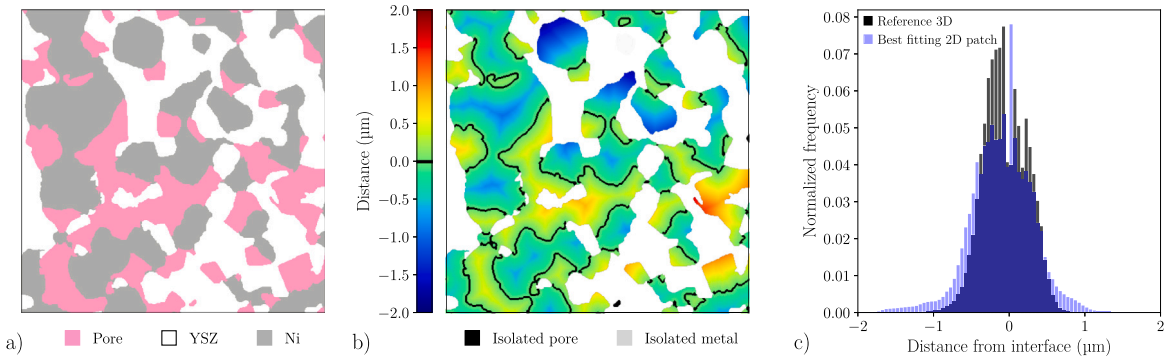

Fig. 2. Most representative geometry of functional layer regarding phase fractions and distance map distribution. (a) Segmented representation with in gray: Ni; in pink: pore; and in white: YSZ (b) Distance map from the Ni/pore interface with the interfaces in black, the Ni in cold colors, the pore in hot colors, the YSZ in white, and the metal and pores that are not connected to an interface in gray and dark gray; (c) Histograms of the 3D reference segmented volume in black and the 2D slice of the synthetic microstructure in transparent blue. (For interpretation of the references to color in this figure legend, the reader is referred to the web version of this article.)

More specifically, the effective interface thicknesses are affected by the calibration of the kinetic constants L_r^{AB} of the Eqs. (16a) and (16b). Particular care was taken to determine these kinetic parameters whilst ensuring a sufficient resolution regarding the chosen mesh. Given the elected W_{AB} and κ_{AB} parameters, the effective interface thicknesses measured in the simulations are about 70 nm at MO interface and 300 nm at OP interface.

The initial values for both ϕ and c variables rely on the distance function from the MO–OP interface, similarly as illustrated in Fig. 2b. The initial NiO layer is imposed thin enough to correspond to a low Degree of Oxidation (typically below 25 wt.%), yet sufficiently thick to ensure numerical stability at the start of the simulation. The initial NiO thickness is set larger in the OP domain than in the MO one, to account for the swelling ratio of NiO (knowing that the boundary between the OP and MO domains is set at the Ni/gas interface in the segmented SEM image or synthetic microstructure).

Regarding the boundary conditions, a zero-flux constraint on the c field is applied at the edge of the YSZ phase, preventing Ni diffusion in the YSZ backbone. A zero-flux condition is imposed on the ϕ field at the OP–YSZ interface, which means that $\nabla\phi = 0$ and results in a $\pi/2$ contact angle between the oxide front and the YSZ surface. This choice corresponds to an intermediate wetting condition given the lack of interfacial energy data in this case. An estimation of this angle on the SEM image after 2 min of oxidation gives an average angle of 92° with a standard deviation of 47°. Because of this uncertainty, a sensitivity analysis has been performed with the model changing the imposed angle. The results have shown that the DoO is almost not affected by the choice of this boundary condition. At the MO-YSZ interface, a Dirichlet condition $\phi = 1$ is prescribed, which allows reproducing the nucleation of an oxide layer all around the Ni particles. SEM observations (Fig. 3a) revealed the formation of a thin NiO layer surrounding Ni particles after a short oxidation time, supporting the use of the Dirichlet condition at the starting point of the simulations. Furthermore, NiO has also been reported at the Ni-YSZ interface after cell operation under various conditions [68,83], while Ni-O bonds are known to dominate the Ni-YSZ interface chemistry [84]. Consequently, a small amount of pre-existing NiO is assumed at the Ni-YSZ interface prior to the modeled case of oxygen introduction causing fast oxidation. The introduction of the NiO layer in the simulation implies a partial compensation of oxide overgrowth, decreasing the effective expansion factor. On the outer edges of the simulated microstructures, periodic boundary conditions are applied for the variables c and ϕ. To enforce periodicity in the simulated geometry, a thin porous layer (approximately 20 nm thick) is added around the geometry.

For the mechanical part of the model, the initial strain is set uniformly to $\varepsilon^{tot}(x, y, t = 0) = 0$. The simulations are performed assuming plane strain conditions applied to the whole 2D microstructure (*i.e.*, the out-of-plane strains ε_{iz} are set to zero). This condition is representative of a 2D cross section taken from a large cell, where deformation in the out-of-plane direction is effectively constrained by the surrounding material. Regarding the boundary conditions applied to the edges of the simulated domain, the displacements are not constrained and only one corner is clamped (in displacement and rotation).

All the parameters involved in the phase field model are listed in Table 1. For each of them, it is reminded if the value is taken from the literature or determined in this study. It can be noticed that the Young's modulus and the diffusion coefficient of Ni in the gas phase have been chosen to low values ($E_P = 0.1$ GPa and $D_P = 1 \times 10^{-22}$ m^2.s^{-1}) in such a way that it does not affect the results.

4. Results and discussion

4.1. Experimental characterization of the cermet oxidation

All the samples, from the pristine to the one oxidized for 120 min, have been characterized by SEM. Fig. 3 presents subregions of the electrode functional layer oxidized for 2 min (Fig. 3a) and 120 min (Fig. 3b). On these images, the bright particles with sharp edges are YSZ, the Ni phase has a slightly darker and less homogeneous gray color with a rougher surface, while NiO appears in dark gray, and pore phase in black.

First, it can be observed that the quantity of NiO increases with the exposition time to air, as expected. The swelling of the Ni particles during their oxidation leads to a sample with a low volume of porosity after 120 min of oxidation at 700 °C. Moreover, the oxide particles present inner nanopores located both at the Ni/NiO interface and within the NiO layer itself. On the 120 min sample (Fig. 3b), cracks can be observed in the YSZ backbone. This indicates that the DoO(t = 2 h) value has exceeded a threshold at which structural damage to the YSZ backbone occurs. Finally, it can be observed that Ni particles are surrounded by an oxide layer from the beginning of the oxidation, even at interfaces with YSZ particles.

The SEM images of samples oxidized for different durations are segmented using a dedicated deep-learning tool developed for this purpose [66]. From these segmented images, the area fractions of Ni and NiO phases are quantified and used to estimate the DoO of each sample with Eq. (2). The experimental DoO extracted from these images is plotted as a function of oxidation time in Fig. 4, for the support and the functional layer. For comparison, the DoO is also calculated using weight measurements of the samples (Fig. 4). It can be seen that the weight-based results closely follow the oxidation trend of the support layer. This result is consistent with the fact that the support accounts

Table 1
Phase field model parameters.

Symbol	Value	Unit	Meaning	Reference
Chemistry				
c_{Ni}^{M}	152 439	mol.m^{-3}	Equilibrium concentration of Ni in metal	[57]
c_{Ni}^{O}	815	mol.m^{-3}	Equilibrium concentration of Ni in oxide	[57]
c_{Ni}^{P}	0	mol.m^{-3}	Equilibrium concentration of Ni in the pore phase	[57]
c_{NiO}^{O}	89 933	mol.m^{-3}	Equilibrium concentration of NiO in oxide	[57]
PBR	1.7231		Pilling–Bedworth ratio $\frac{V_m^{NiO}}{V_m^{Ni}} = \frac{c_{Ni}^{M}}{c_{NiO}^{O}}$	[57]
ρ_M	8902	kg.m^{-3}	Theoretical density of Ni	[85]
ρ_O	6720	kg.m^{-3}	Theoretical density of NiO	[85]
Diffusion				
T	973	K	Temperature	Chosen
D_M	1.6×10^{-19}	m^2.s^{-1}	Diffusion coefficient of Ni in the metal	[86]
D_O	8×10^{-16}	m^2.s^{-1}	Diffusion coefficient of Ni in the oxide	Identified
D_P	1×10^{-22}	m^2.s^{-1}	Diffusion coefficient of Ni in the pore phase	Chosen
Interfacial				
κ_{MO}	3.36	J.m^{-1}	Coefficient of the gradient term of the interface MO	Chosen
κ_{OP}	6.4	J.m^{-1}	Coefficient of the gradient term of the interface OP	Chosen
W_{MO}	1.16×10^{7}	J.m^{-3}	Height of the MO energy barrier	Chosen
W_{OP}	2.76×10^{6}	J.m^{-3}	Height of the OP energy barrier	Chosen
k	10^{3}	J.m^{-3}	Curvature of chemical energy square functions	Identified
L_ϕ	1.6×10^{-4}	J^{-1}.m^3.s^{-1}	Mobility coefficient for ϕ interface	Identified
L_r^{MO}	10^{5}	s^{-1}	Kinetic constant of the MO interface reaction	Identified
L_r^{OP}	1.6×10^{8}	s^{-1}	Kinetic constant of the oxidation reaction	Identified
Mechanics				
E_M	173	GPa	Young's modulus of Ni	[87]
E_O	175	GPa	Young's modulus of NiO	[88]
E_P	0.1	GPa	Young's modulus of the pore phase	[57]
E_{YSZ}	220	GPa	Young's modulus of YSZ phase	[57]
ν_M	0.325		Poisson ratio of Ni	[89]
ν_O	0.3		Poisson ratio of NiO	[89]
ν_P	0.3		Poisson ratio of the pore phase	[57]
ν_{YSZ}	0.32		Poisson ratio of YSZ phase	[57]
ϵ_0^g	0.002		Growth strain constant	Identified

for around 90 % of the total electrode thickness and thus dominates the cell mass. For each point, horizontal error bars were traced to represent the potential uncertainty in the oxidation time. To quantify the DoO, the segmentation was performed on large samples (about 90 µm × 30 µm for each layer) that can be considered as representative of the microstructure of the whole layer. The DoO error bars reported for each oxidation time along the y-axis represent the uncertainty coming from the segmentation, quantified as the standard deviation of the experimental DoO obtained from an ensemble of segmentation results. For each oxidation time, the image segmentation was performed independently using ten different U-Net models previously trained and validated for uncertainty quantification [66]. This procedure yields ten distinct segmentation maps for the same image, from which ten corresponding DoO values are computed. The obtained standard deviations stand below 0.75 wt.%, averaging 0.3 wt.% for the functional layer and 0.4 wt.% for the support layer, which makes them difficult to distinguish from the symbols on the graph. The DoO may be affected by additional sources of error coming for example from experimental manufacturing and measurement that cannot be quantified here.

In line with the observations of Laurencin et al. [49], the experimental results show parabolic oxidation kinetics for both layers. This behavior is characteristic of diffusion-controlled oxide growth [90], resulting from the increasing diffusion path length for Ni ions into NiO as the oxide layer thickens. In addition, the tested microstructures have a Gaussian-like MO–OP distance histogram, as illustrated by Fig. 2c, which means that progressively the oxide can grow in fewer Ni and porosity regions. This microstructural feature tends to slow down the parabolic oxidation kinetics.

It is worth noting that the DoO for the two layers tends to an upper bound for long reoxidation time. This asymptotic limit is not the same for the two layers, as observed in Fig. 4. After 120 min of oxidation time, the DoO is measured at 80 wt.% in the support and 60 wt.% in the functional layer. This difference of behavior is related to the difference of initial porosity between the two layers (in its as-manufactured, pre-reduction state, the functional layer is fully dense in its oxidized state while the support is already porous). Regarding the functional layer, the reoxidation stops when the pores are completely filled. Indeed, at this stage, it is worth noting that a fraction of the reduced Ni remains not oxidized. This phenomenon is explained by the overswelling due to the NiO sponge-like structure so that the nanoporous NiO takes up more space than the initial dense NiO (of the as-manufactured, pre-reduction state). Therefore, the additional porosity in the support allows reaching higher DoO. Using the SEM images, the effective Ni to NiO volume change during reoxidation has been estimated by measuring the volume fraction of the nanoporous NiO. This ratio is found to be around 1.9, which is similar to the value of 1.92 reported by De Angelis et al. [16].

4.2. Model validation

4.2.1. Comparison with experiments

For the simulations, two 10 × 10 µm^2 geometries were selected from the support layer and two others from the functional layer, all extracted from large segmented SEM images. In addition, one 10 × 10 µm^2 slice taken from a representative 3D artificial microstructure of each layer (support and functional) was selected to assess the agreement between phase field simulations performed on real and synthetic cermets. All selected geometries were chosen to best represent the characteristic phase fractions and distance-map distributions of each layer. The phase volume fraction and equivalent mean particle diameter for each phase of the simulated geometries are reported in tables S-2.1 and S-2.2 of the supplementary material section S-2.

A representative example of a synthetic functional layer is shown at its initialized state in Fig. 5 with labels of MO, OP and YSZ domains, and colored areas of Ni, nanoporous NiO, pore, and YSZ phases. In the

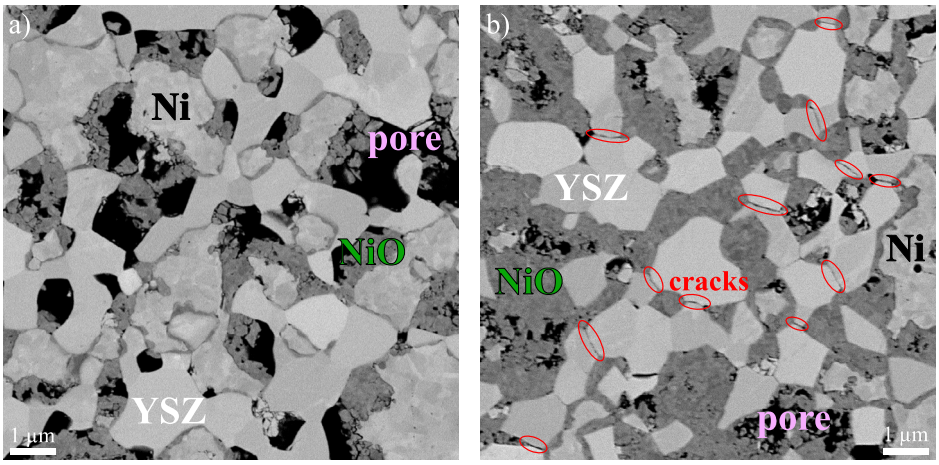

Fig. 3. SEM images ($10 \times 10\,\mu m^2$) of the functional layer of samples oxidized in air at 700 °C for (a) 2 min (b) 120 min.

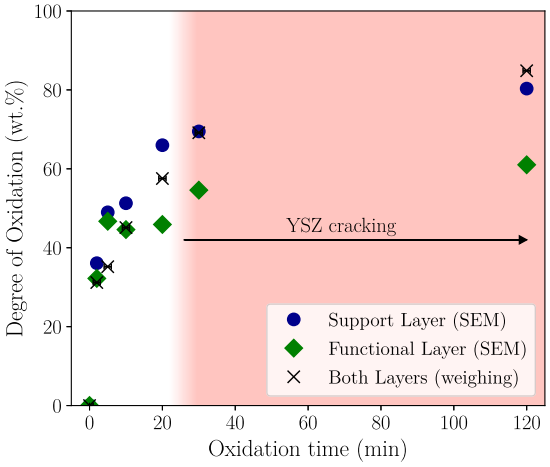

Fig. 4. Experimental Degree of Oxidation of nickel in the cermet as a function of air exposure time at 700 °C obtained from cell weighing (black), and segmented SEM image of the supported layer (blue) and the functional layer (green). The oxidation time when YSZ cracks start to appear is in transparent red.

initial state, the imposed Dirichlet boundary condition produces a thin NiO shell (green border) around all Ni particles, corresponding to a DoO in the range of 15 wt.% to 25 wt.% (here 16 wt.%) although the layer thickness is only about 100 nm. Thus, the evolution of the DoO as a function of oxidation time starts from this initial oxidation for the simulated results. Nevertheless, it is worth reminding that this initial thin layer surrounding the reduced Ni particles is consistent with the observations of the cermet microstructure at an early stage of oxidation (see Section 4.1).

After 2 min of simulated oxidation (Fig. 5), the DoO reaches 32 wt.%. At this stage, the oxidation front is non-uniform, depending on the local curvature and position of the MO and OP interfaces. The average thickness of the oxide layer is around 280 nm. The simulated microstructure matches the experimental one depicted in Fig. 3a after 2 min of oxidation, showing significant NiO growth within the pores, consistent with parabolic oxidation kinetics. After 120 min (Fig. 5), the DoO reaches 60 wt.%, and the nanoporous NiO phase (green phase) fills most of the pores, although a substantial amount of metallic Ni remains. The result of the simulation is in agreement with the experimental observations shown in Fig. 3b, where non-oxidized Ni is still visible and few pores also remain.

Fig. 6 compares the time evolution of DoO for simulations performed on both functional and support layer microstructures with the corresponding experimental data. Overall, the simulations reproduce the parabolic kinetics and asymptotic behavior observed experimentally for both layers. The results for the support layer deviate slightly more from the experimental curve than the functional layer ones, likely due to the difficulty of capturing large pores and particles (Fig.S-1.1) within 2D $10 \times 10\,\mu m^2$ microstructures. Simulations performed on the representative synthetic geometries closely follow those obtained from the segmented ones.

Model parameters listed as "Identified" in Table 1 were calibrated by trial and error to reproduce as closely as possible the experimental oxidation kinetics of the functional layer, while remaining within physically realistic ranges for the diffusion coefficient of Ni in the oxide D_O. This calibration was performed using the two real segmented images of the functional layer (Fig. 6). Then, the model validity was assessed by simulating the other microstructures without changing the fitted data. On Fig. 6, it can be observed that the same model parametrization is also able to catch the kinetic of the support layer using the real segmented microstructures. This demonstrates that the model correctly captures the effect of a microstructural change on the oxidation kinetics. Moreover, the simulated DoO as a function of time for the synthetic microstructures also matches the experimental data for both layers. The statement also demonstrates the model capability to simulate correctly oxidation on different microstructures which are representative of the real cermet but with different local geometry.

The expansion factor η_{eff} has been calculated from the simulations for the functional layer considering only the oxide growth occurring after initialization. After 120 min of oxidation, this ratio is equal to about $\eta_{eff} = 2.5$. This value does not reach the upper bound of 2.7 since a fraction of the diffusible Ni remains stored in the NiO rather than being converted into oxide. When the entire simulation is considered, the overall measured expansion ratio further decreases to around 2.05, close to the experimental ones slightly above 1.9. This decrease is explained by taking into account the pre-existing NiO layer introduced at MO-YSZ interfaces during initialization. It shows that even without explicitly modeling nanopores in the NiO phase, the simulations capture accurately the oxidation kinetics including the saturation of the DoO versus time due to the particle overswelling.

4.2.2. Ni diffusion coefficient in NiO

Among the identified parameters, the Ni diffusion coefficient in NiO D_O is of key importance as it governs the NiO growth. A sensitivity analysis on this parameter has been performed by varying its value in simulations. Since the model is built as diffusion-dependent, the modification of this property acts as a scaling factor on the evolution of DoO versus time, without affecting the ultimately reached asymptotic value of DoO. The calibration of this parameter on the evolution of

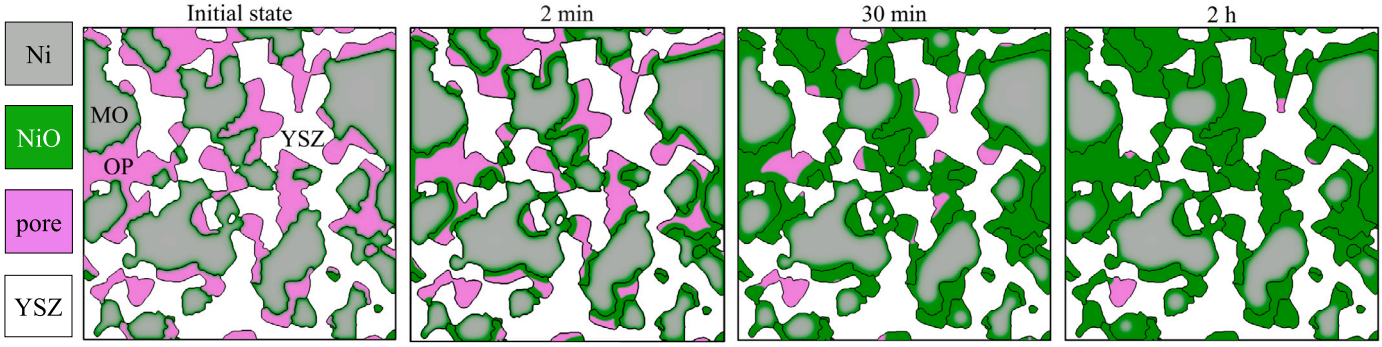

Fig. 5. Phase distribution of 2D simulation of oxidation on a $10 \times 10\,\mu m^2$ functional layer synthetic microstructure for oxidation times of 0; 2; 30 and 120 min. The initial domains are represented on the left image at initial state. The phases are represented in gray for Ni, green for NiO, pink for the pore phase, and white for YSZ. (For interpretation of the references to color in this figure legend, the reader is referred to the web version of this article.)

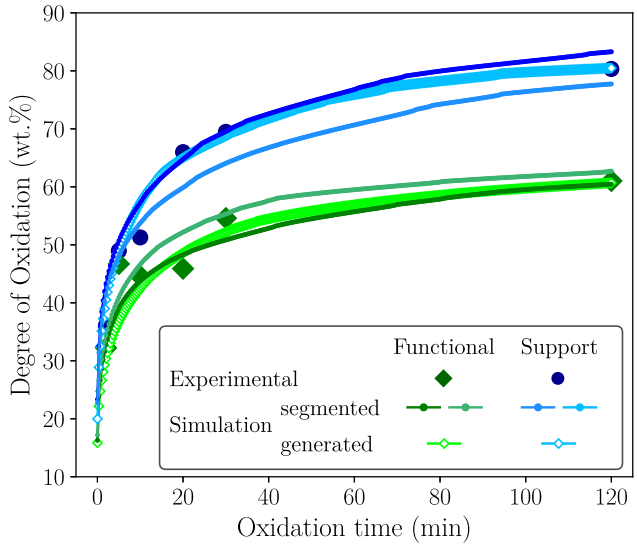

Fig. 6. Experimental and simulated Degree of Oxidation of nickel as a function of air exposure time for functional and support microstructures. Large dots curves are experimental data, three representative geometries are used for the simulations. The results obtained from simulations on generated geometries for both layers appear in light green and light blue with hollow diamonds instead of points. (For interpretation of the references to color in this figure legend, the reader is referred to the web version of this article.)

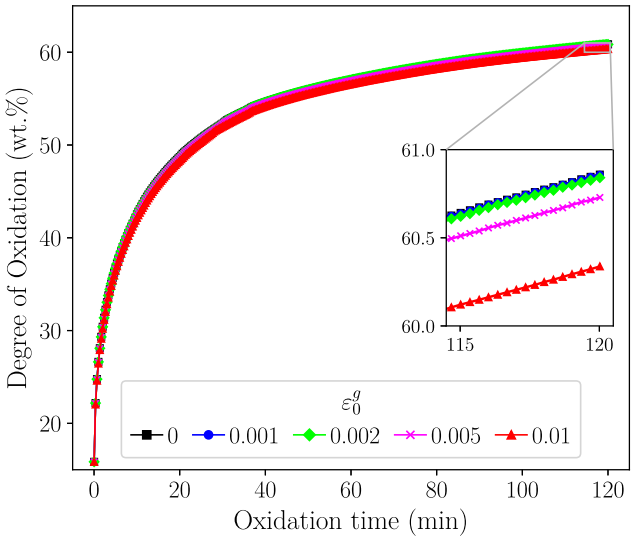

Fig. 7. Kinetics of functional layer microstructures with different values of growth strain constant ε_0^g.

DoO as a function of reoxidation time for both layers leads to the value: $D_O = 8{\times}10^{-16}\,m^2.s^{-1}$ with a rather narrow uncertainty range extending from $5.6 \times 10^{-16}\,m^2.s^{-1}$ to $1.2 \times 10^{-15}\,m^2.s^{-1}$. These bounds correspond to the values that keep the experimental value of DoO ($t = 120$ min) within the envelope of the simulated DoO curves. Because of the high heterogeneity of the microstructure, the coefficient of diffusion of Ni in NiO may vary but we did not consider a heterogeneous distribution of its values here. The morphologies of each simulated microstructure before and after 120 min of oxidation are provided in the supplementary material section S-3.

In the literature, the value for the Ni diffusion coefficient in NiO can change by orders of magnitude since it is highly dependent on the diffusion path. Peraldi et al. [41] and Atkinson et al. [21,22] conducted measurements to distinguish diffusion through the bulk, dislocations and grain boundaries. In practice, Ni transport across the oxide scale involves contributions from all these mechanisms. As summarized in [41], the diffusion coefficient of Ni in NiO at 700 °C typically lies in the range $10^{-17}\,m^2.s^{-1} < D_O < 10^{-14}\,m^2.s^{-1}$. For the model calibration, the identified diffusion coefficient has been found to be $D_O = 8{\times}10^{-16}\,m^2.s^{-1}$, which is in the range of predominant diffusion along crystallographic grain boundaries and dislocations. Lin et al. [57] proposed a relation linking the effective diffusion coefficient of Ni in NiO to the relative contributions of bulk and grain boundary diffusion, dependent of the grain diameter of NiO and the grain boundary width. Using this relation with the value of D_O identified in our study and the grain boundary width proposed by Lin et al., we obtain a NiO grain equivalent diameter of about 45 nm. This value appears plausible, although the complex topology of Ni in H_2 electrodes likely results in a more heterogeneous NiO grain structure than that captured by this simple formula.

4.2.3. *Stress state in the cermet and influence on the oxidation kinetics*

As described in the model section, the oxide growth strain is implemented as an inelastic in-plane strain defined by a constant value in the oxide layer. This uniform strain assumption is justified by the difficulty of estimating the spatial distribution of the growth strain due to the complex and heterogeneous nature of the growing oxide microstructure. The generated microstructure of functional layer used in Fig. 5 is reused here to simulate oxidation for five growth strain values: $\varepsilon_0^g = 0$; 0.001; 0.002 (used for simulations in the previous section) ; 0.005; and 0.01.

First, the influence of the growth strain constant on oxidation kinetics has been assessed. The results of DoO kinetics for the studied cases are gathered in Fig. 7. The oxidation curves for $\varepsilon_0^g = 0$ and $\varepsilon_0^g = 0.002$ are almost identical, with the latter reaching a slightly lower

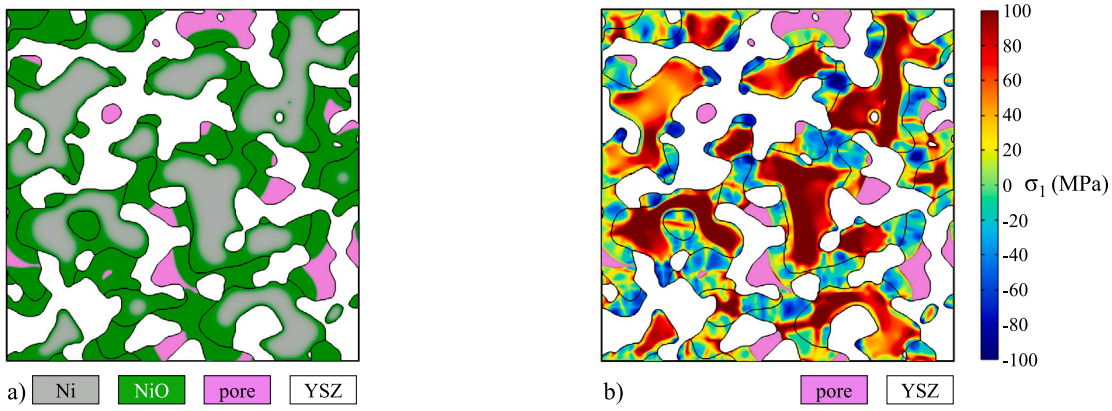

Fig. 8. Microstructure after 30 min of oxidation in the $\epsilon_0^g = 0.002$ case. Results of (a) phase distribution and (b) first principal stress σ_1 in Ni and NiO map.

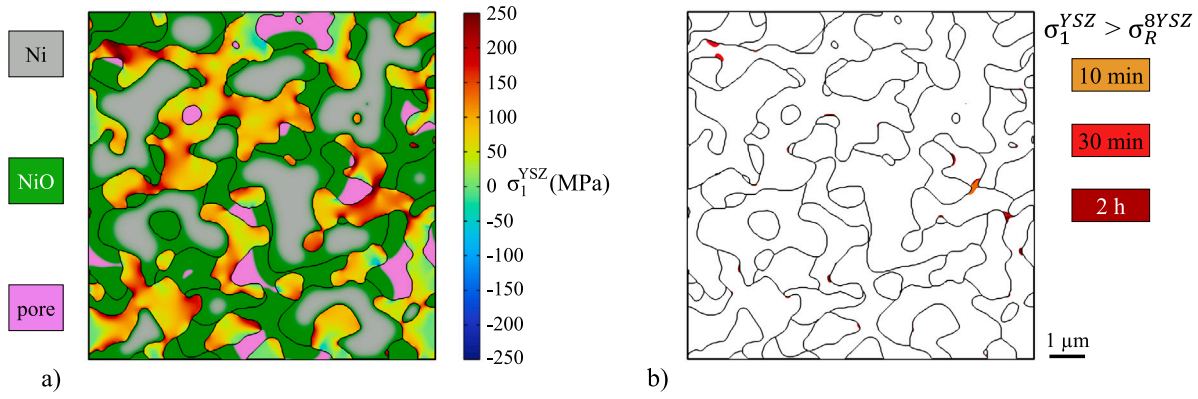

Fig. 9. (a) Combined phases distribution and first principal stress in YSZ σ_1^{YSZ} map (b) Map of the areas of 8YSZ in which the first principal stress is larger than a typical value of 8YSZ strength (in the $\epsilon_0^g = 0.002$ case). Three maps are superimposed: in orange for the 10 min map ; red for 30 min and dark red for 2 h. (For interpretation of the references to color in this figure legend, the reader is referred to the web version of this article.)

final DoO (about 0.02 wt.% lower). The largest ϵ_0^g tested (0.01) leads to a slight difference in the oxide morphology, while the DoO is only around 0.5 wt.% lower than the non-strained one. In this case, the imposed strain is sufficiently high so that the mechanical term involved in the free energy functional slightly slows down the oxide growth. It can thus be inferred from this sensitivity analysis that in this range, the imposed strain has only a limited influence on the oxidation kinetic rate. In other words, the mechanical part of the functional could even be omitted to quantify the oxidation rate even though it is capital to compute the stress state in the cermet.

The simulated microstructure is displayed in the case $\epsilon_0^g = 0.002$ after 30 min of oxidation in Fig. 8a with the corresponding first principal stress σ_1 in Ni and NiO in Fig. 8b. Because of the inelastic growth strain applied in the oxide, it has been found that the Ni is subjected to a tensile stress. On the contrary, the NiO phase, which is constrained by both the Ni and YSZ, is under compression. The average of the first principal stress in the Ni layer $\overline{\sigma_1^{Ni}}$ is around 87 MPa at 30 min of oxidation. Because of the complex microstructure, the stress state in NiO is quite heterogeneous, with a majority of compressive stress (averaging −30 MPa), and local tensile areas, as shown in Fig. 8a. The parts of the NiO layer subjected to local tensile stress are close to very convex Ni/NiO interfaces, as discussed in [32,79]. This heterogeneous stress distribution could even lead to some delamination and/or cracking of the NiO as already reported in other studies [14,37,39,40]. The current formulation captures the effect of interface curvature through the local orientation of the phase field gradient. However, the implementation of growth strain is limited to the definition of ε^g in Eq. (23) without explicitly including additional geometric growth contributions such as the ones reported in [32,91,92]. This choice is motivated by the fact that other NiO film mechanisms (delamination, pore forming and cracking) are not explicitly modeled as NiO is described as a homogeneous phase.

The phase distribution is presented in Fig. 9a together with the first principal stress in YSZ (σ_1^{YSZ}) for the case $\epsilon_0^g = 0.002$ after 30 min of oxidation. At this stage, the YSZ phase undergoes a rather low tensile stress in average with a mean value of 90 MPa. Due to the heterogeneous microstructure, several necks in the YSZ backbone are subjected to locally high tensile stresses that exceed the fracture strength of 8YSZ (*i.e.*, around 245 MPa [62]) for millimetric samples, no size effect is taken into account here.

Assuming that such stress concentration can yield the formation of micro-cracks, we aim to follow the density of cracks as a function of oxidation time. To do so, Fig. 9b shows the regions of 8YSZ where the first principal stress is larger than the strength in the $\epsilon_0^g = 0.002$ case. As expected, the density of these critical regions increases with oxidation time. After 30 min, two necks of the YSZ backbone exhibit tensile stresses exceeding the theoretical strength, making them potential crack initiation sites. In addition, several smaller regions also satisfy the strength criterion without spanning an entire YSZ neck and may also contribute to crack initiation.

Since fracture initiation is not only led by a strength criterion but also by an energy criterion, which means that exceeding the strength does not necessarily produce a crack [93], this approach cannot predict the amount of cracks that may form. Nevertheless, to assess our model and the values of ϵ_0^g, we analyze, for all tested cases, the areas subjected to tensile stresses higher than the 8YSZ strength.

Fig. 10a reports the evolution of the fraction of 8YSZ area where the tensile stress exceeds the 8YSZ strength for all ϵ_0^g cases. From these maps, we estimate the potential number of cracks by detecting the

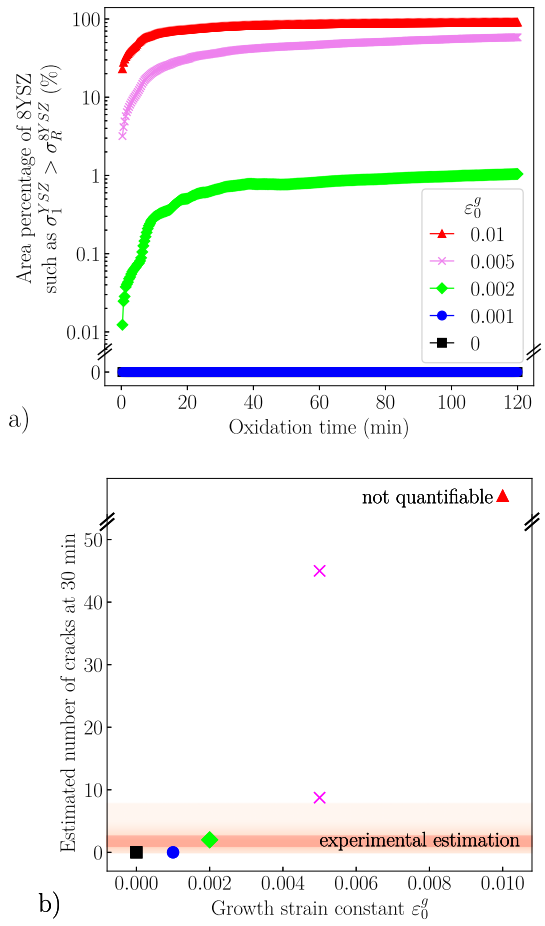

Fig. 10. (a) Graph of the percentage of 8YSZ area above 8YSZ strength for each value of ϵ_0^g. (b) Amount of estimated cracks at 30 min as a function of ϵ_0^g. This value of crack density for a $10 \times 10\,\mu m^2$ square was experimentally measured. The range for which the distribution of cracks per tile overcomes 15 % is in red, while the whole distribution appears at a lower color intensity. (For interpretation of the references to color in this figure legend, the reader is referred to the web version of this article.)

necks where the strength criterion is exceeded and setting a protective layer of about 300 nm around each crack, within which no additional crack can form. The resulting number of potential cracks after 30 min of oxidation is reported in Fig. 10b. This oxidation time was chosen because it corresponds to the experimental threshold at which the first cracks were observed.

For $\epsilon_0^g = 0$ and 0.001 cases, the entire YSZ backbone is subjected to stresses lower than 8YSZ strength, which should not lead to any crack (Fig. 10a and b). In the $\epsilon_0^g = 0.002$ case, the fraction of YSZ exceeding the strength increases with oxidation time, leading to a first potential crack slightly before 10 min of oxidation and a second one before 30 min, with a possible third one in the upper left corner of the geometry because of large initiation zones in a narrow neck (Figs. 10a and 9b). The $\epsilon_0^g = 0.005$ and 0.01 cases exhibit a large fraction of YSZ already above the critical tensile stress from the early stages of oxidation. An incremental analysis of the maps allows to estimate the number of cracks in the range of 45 after 30 min of oxidation for $\epsilon_0^g = 0.005$. The same approach could not be applied to the $\epsilon_0^g = 0.01$ case because an excessively large fraction of the YSZ phase is already subjected to high tensile stresses from the very beginning of oxidation, preventing the identification of distinct crack sites (Fig. 10b).

The estimated number of cracks at 30 min (Fig. 10b) can be compared to experimental observations. SEM image analysis was conducted on about $18\,000\,\mu m^2$ of the electrode functional layer to detect cracks in the YSZ backbone. The density of cracks averaged 1.9 cracks per $10 \times 10\,\mu m^2$ tile with a variability depending on the local phase composition and geometry. In Fig. 10b is traced in transparent red the area in which the distribution of cracks per tile overcame 15 % and in a clearer color is represented the whole distribution with its intensity proportional to its frequency. This crack density range is in best agreement with the $\epsilon_0^g = 0.002$ case. This result confirms that $\epsilon_0^g = 0.002$ provides the most realistic representation of the experimental behavior among the tested values.

It is well known that the appearance of cracks in the YSZ backbone has an impact on the electrode operation [67]. Indeed, the damage of the YSZ phase contributes to increase the mean ionic diffusion path. In other words, the tortuosity factor for the backbone increases with the number of cracks. Nevertheless, damage to the YSZ backbone can also lead to non-percolated regions that will decrease the density of active TPBs. In this way, the two predicted cracks with the model after 30 min of oxidation (Fig. 10b) could lead to lower electrode performances. A precise estimation of these consequences requires coupling the result of the present phase field model with an electrochemical model, which is beyond the scope of the present work. Therefore, a preliminary study of the impact of the simulated cracks on YSZ connectivity is provided in the supplementary material section S-4. This estimation suggests that even a limited number of cracks in the YSZ backbone reduces its connectivity and the number of active TPBs, resulting in performance loss and highlighting the importance of preventing YSZ backbone fracture.

However, the current simulation framework can only provide a rough estimation of crack formation in the microstructure. In particular, the true growth strain may differ from our simplifying assumptions. Its direction may not be purely in-plane, as suggested by NiO grain growth, and it may increase during oxidation even under the simple Rhines theory [42]. Refining the growth-strain definition would require lower-scale modeling and additional experimental data. Ultimately, the prediction of crack onset and propagation within the microstructure must rely on models that take into account stress and energy criteria such as the fracture phase field methods [94].

4.3. Impact of microstructure on oxidation

Generated artificial microstructures were used to evaluate the effect of Ni particles size on the oxidation of the functional layer for which the porosity is only due to NiO reduction to Ni (see Section 2.1). For this study, the same settings were kept to generate the 3D microstructures (*i.e.*, same phase volume fractions and YSZ particle size), except for the Ni mean particle diameter. The geometries were selected in such a way that their measured phase fractions deviated by less than 1 % from the prescribed values and with an equivalent diameter for YSZ close enough to the target value. The microstructural properties measured on these geometries are provided in the supplementary material section S-2. The Ni mean particle diameter changes from 1.56 µm for the coarsest microstructure to 0.67 µm for the finest one. On the contrary, the mean pore size exhibits only limited variation. This microstructural change mimics the Ni agglomeration that occurs during SOC operation [95,96]. In addition, the smallest particle-size range investigated can provide insights for emerging nanostructured electrodes [97].

In Fig. 11a, the DoO of each microstructure is plotted as a function of oxidation time. The simulated microstructures in their initial state and after 2 h of oxidation are displayed in the supplementary material section S-3. For all microstructures, a parabolic oxidation behavior is obtained, with a systematically faster oxidation for smaller Ni particles. Each of the curves were fitted using an Avrami equation [98]:

$$DoO(t) = DoO_{\max}(1 - \exp(-kt^n)) \tag{25}$$

It appears that the fit curves displayed in dotted lines on Fig. 11a match the simulated data, with only a small deviation for the short

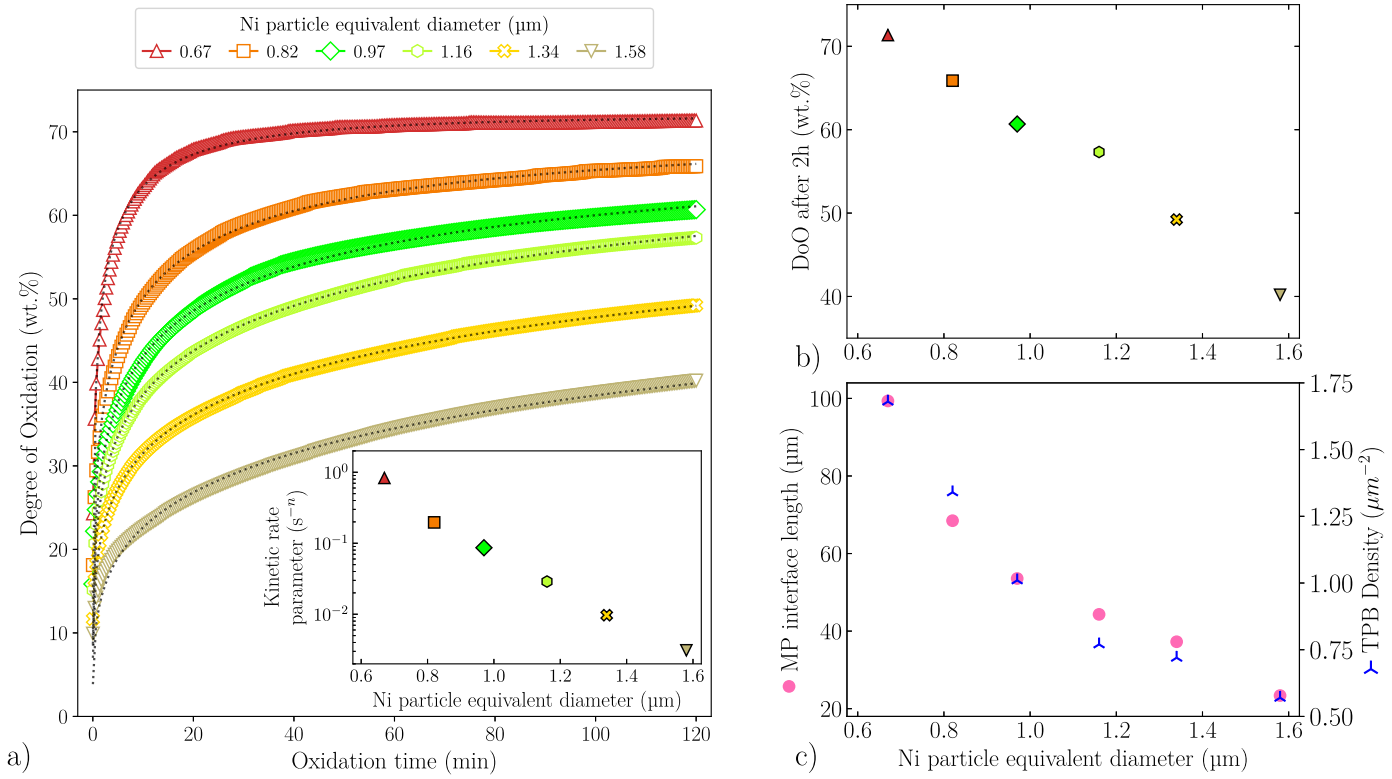

Fig. 11. (a) Oxidation kinetics of functional layer microstructures with varying equivalent Ni particle average equivalent diameter. Dotted lines represent Avrami fits. The inset shows the kinetic rate parameter in log scale as a function of the Ni particle equivalent diameter. (b) Final DoO after 120 min of oxidation as a function of the Ni particle equivalent diameter. (c) Initial Ni–pore interface length and TPB density traced as a function of the Ni particle equivalent diameter.

oxidation times of coarser geometries. The saturation level $DoO_{\max}$ obtained from the fit is similar for all cases (around 72 wt.%). This is because the microstructures have a very similar surface fraction ratio $R_{\mathrm{PM}} = \frac{Area(P)}{Area(M)}$, with areas corrected to exclude unconnected regions. The Avrami exponent n has a value close to 0.3 for every fit, since the NiO growth mechanism, controlled by Ni diffusion into NiO, is the same for all these curves. The values of kinetic rate parameter k for every curve are given in the inset of Fig. 11a as a function of the Ni particle equivalent diameter. The kinetic parameter k is found to strongly decrease with increasing the Ni particle diameter. The DoO value after 2 h of oxidation is also plotted in Fig. 11b as a function of d_{Ni}. This DoO ($t = 2\,\mathrm{h}$) is inversely proportional to the Ni particle equivalent diameter. The evolution of k and DoO ($t = 2\,\mathrm{h}$) with the Ni particle size can be explained by the longer Ni diffusion path for the bigger Ni particle that limits the overall kinetic. In other words, high oxidability correlates with a high surface-to-volume ratio (here perimeter-to-area ratio) of Ni particles, which is directly linked to small equivalent Ni diameters. Since these ratios are inversely proportional to the diameter of Ni, the latter appears as a relevant indicator for oxidation kinetics. From this analysis, it appears that increasing the Ni particle size (or decreasing the surface-to-volume ratio) could be an interesting mitigation strategy to improve the cermet tolerance to oxidation. However, it is well established [97,99] that increasing the Ni particle size has a highly detrimental impact on the electrode performance. In the studied microstructures, the TPB density is divided by three between the lowest and the highest Ni particle dimensions (see supplementary material section S-5). This difference strongly affects the performance since TPB density governs the electrochemical reaction in this electrode. Thereby, a trade-off has to be found between the cermet tolerance to Ni oxidation for long-term durability and high density of TPBs to ensure the best initial electrochemical performances.

To complement the study, the effect of modifying the volume fractions is assessed by simulating oxidation on two additional support-layer microstructures ($R_{\mathrm{PM}}^{Support} \approx 1.1$) in addition to the already simulated functional layers ($R_{\mathrm{PM}}^{Functional} \approx 0.6$). Although $R_{\mathrm{PM}}^{Support} > R_{\mathrm{PM}}^{Functional}$, the oxidation in the simulated supports is still limited by the lack of porosity so that the DoO at saturation is still below 100 wt.% (here $DoO_{\max} = 92\,\mathrm{wt.\%}$). To evaluate the oxidation tolerance as a function of the microstructure, we need to introduce a descriptor that takes into account the volume fraction and the particle size. However, many different methods can be used to evaluate the mean Ni particle equivalent diameter d_{Ni} in complex microstructures, providing different values for this metric. To overcome this issue, we define the descriptor, named microstructural interface parameter as follows $\Lambda_{\mathrm{PM}} = R_{\mathrm{PM}}\sqrt{l_{\mathrm{PM}}}$ where l_{PM} is the initial Ni–pore interface length. This interface length l_{PM} parameter is directly linked to the surface-to-volume ratio and therefore to diffusion-driven oxidation mechanisms. The values of l_{PM} are plotted in Fig. 11c against d_{Ni}. The interface length decreases strongly as the Ni particle diameter increases, following a logarithmic trend which illustrates that larger Ni particles tend to reduce the initial oxidation interface. The TPB density of each microstructure was measured and reported against d_{Ni} in Fig. 11c. Interestingly, its evolution with d_{Ni} follows a very similar trend to that of l_{PM}, showing that the reduction of the Nickel–pore interface is strongly tied to the reduction of TPBs. Notably, l_{PM} is closely linked to oxidation kinetics, as it defines the length of the initial oxidation reaction, while TPB density governs electrochemical reactions. This evidences a strong coupling between fast oxidation and high performance for the type of microstructures studied here. Therefore, further work should explore other types of microstructures to decorrelate oxidation kinetics from performance, or to determine whether cracking can be avoided despite fast oxidation kinetics.

The DoO at $t = 2\,\mathrm{h}$ has been plotted as a function of the microstructural interface parameter Λ_{PM} in Fig. 12 for all the generated

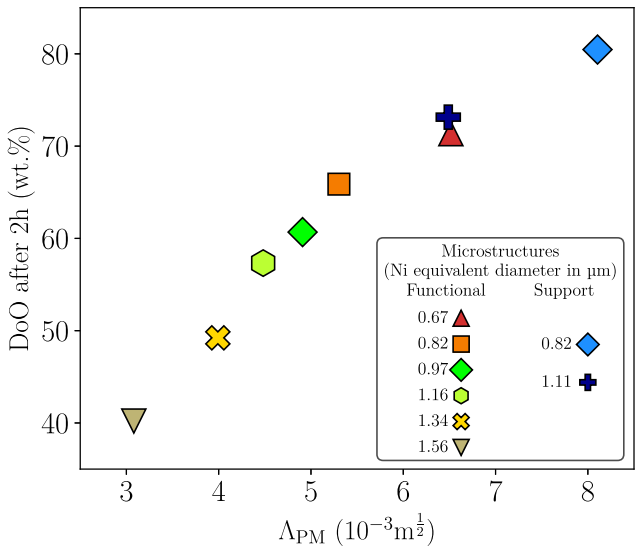

Fig. 12. DoO after 120 min of oxidation plotted as a function of the normalized microstructural interface parameter for different microstructures, including functional and support layers with various Ni particle sizes.

microstructures including the functional layer and support. It can be seen that all the points are well aligned along a linear trend ($R^2 = 0.95$) demonstrating the relevance of the proposed indicator. This curve could be used to evaluate the $DoO(t = 2\,\mathrm{h})$ for cermet microstructures with varying phase fractions, particle sizes, shapes, at least within the explored parameter range. Therefore, it represents a useful tool to start exploring microstructure characteristics optimization.

5. Conclusions and perspectives

This work establishes a validated phase field model for outward oxidation in Ni-YSZ cermets, integrating microstructural evolution, diffusion-controlled kinetics, oxidation-induced swelling and mechanical stress development in these microstructures. The model demonstrated its ability to replicate experimental oxidation kinetics across synthetic and real initial microstructures of Ni, pore and YSZ. Its calibration allowed us to identify the diffusion coefficient of Ni in NiO governing the parabolic kinetics and to estimate the relative contributions of dominating grain-boundary and dominated bulk diffusion in NiO.

Beyond validation, the model reveals critical microstructure-kinetics relationships. Ni particles coarsening tends to significantly slow down the oxidation kinetic rate, a direct consequence of the surfacic reaction mechanism of oxidation. The link between oxidation and microstructural features was explored, allowing the definition of a microstructure descriptor (combining phase fractions and initial oxidation interfaces) which correlates with the final DoO. This descriptor could be used to estimate oxidation kinetics prior to simulation, and therefore to allow faster microstructure analysis and optimization.

The implementation of growth strain allowed estimation of the heterogeneous stress distribution in the Ni and NiO, and more importantly in the YSZ backbone. The simulations have revealed compressive stresses in NiO, consistent with the limited experimental information available from similar cases. However, heterogeneities in the microstructure can yield local tensile stress in the NiO that may result in NiO damage as observed experimentally. The value of the growth strain constant was calibrated to correspond to the experimental threshold cracking time of around 30 min for the functional layer. In the 8YSZ backbone, simulations result in local tensile stress peaks of a magnitude compatible with crack initiation at 8YSZ necks. To better predict the crack density evolution in the cermet, a phase field fracture model could be coupled to our oxidation model, which could also be improved by refining the current implementation of growth strain. The updated model will constitute an efficient tool to identify new redox-tolerant microstructures and materials to enhance SOCs durability.

CRediT authorship contribution statement

Sylvain Fournier: Writing – original draft, Visualization, Software, Methodology, Investigation, Formal analysis, Conceptualization. **Maxime Hubert:** Writing – review & editing, Resources, Project administration, Methodology, Funding acquisition, Conceptualization. **Kassem Dia:** Writing – review & editing, Software, Methodology, Investigation. **Thomas David:** Resources, Methodology, Investigation. **Aurélien Doitrand:** Writing – review & editing, Conceptualization, Methodology. **Gergely Molnár:** Writing – review & editing, Conceptualization, Methodology. **Sylvain Meille:** Writing – review & editing, Conceptualization, Methodology. **Jérôme Laurencin:** Writing – review & editing, Project administration, Funding acquisition, Conceptualization.

Declaration of competing interest

The authors declare that they have no known competing financial interests or personal relationships that could have appeared to influence the work reported in this paper.

Acknowledgment

The authors gratefully acknowledge financial support through the MatCHMaker project which has received funding from the European Union's Horizon Europe research and innovation program under grant agreement N° 101091687.

Appendix A. Developed form of the governing equations

The Allen–Cahn equation (14) is expressed as a function of the derivative of the Gibbs free energy with respect to ϕ. This term can be developed as follows:

$$\frac{\delta G}{\delta \phi} = \frac{\partial f^{Ni}_{\mathrm{chem}}}{\partial \phi} + \frac{\partial f^{\phi}_{\mathrm{chem}}}{\partial \phi} - \nabla \cdot \frac{\partial f_{\mathrm{grad}}}{\partial(\nabla \phi)} + \frac{\partial f_{\mathrm{mecha}}}{\partial \phi}. \tag{A.1}$$

with each term being:

$$\frac{\partial f^{Ni}_{\mathrm{chem}}}{\partial \phi} = \frac{1}{2}\left[-i_{\mathrm{MO}}\frac{\mathrm{d}p}{\mathrm{d}\phi}k_{\mathrm{M}}\left(c - c_{\mathrm{M}}\right)^2 + \frac{\mathrm{d}p}{\mathrm{d}\phi}k_{\mathrm{O}}\left(c - c_{\mathrm{O}}\right)^2 - i_{\mathrm{OP}}\frac{\mathrm{d}p}{\mathrm{d}\phi}k_{\mathrm{P}}\left(c - c_{\mathrm{P}}\right)^2\right] \tag{A.2}$$

$$\frac{\partial f^{\phi}_{\mathrm{chem}}}{\partial \phi} = (i_{\mathrm{MO}}W_{\mathrm{MO}} + i_{\mathrm{OP}}W_{\mathrm{OP}})\frac{\mathrm{dg}}{\mathrm{d}\phi} \tag{A.3}$$

$$-\nabla \cdot \frac{\partial f_{\mathrm{grad}}}{\partial(\nabla \phi)} = -(i_{\mathrm{MO}}\kappa_{\mathrm{MO}} + i_{\mathrm{OP}}\kappa_{\mathrm{OP}})\nabla^2\phi \tag{A.4}$$

$$\frac{\partial f_{\mathrm{mecha}}}{\partial \phi} = \frac{1}{2}\frac{\partial C_{\mathrm{ijkl}}}{\partial \phi}\varepsilon^{el}_{\mathrm{ij}}\varepsilon^{el}_{\mathrm{kl}} + \frac{\partial \varepsilon^{el}_{\mathrm{ij}}}{\partial \phi}C_{\mathrm{ijkl}}\varepsilon^{el}_{\mathrm{kl}}. \tag{A.5}$$

The terms of the derivative of the elastic energy are developed in the following:

$$\begin{aligned}\frac{1}{2}\varepsilon_{ij}^{elT}\frac{\partial C_{ijkl}}{\partial\phi}\varepsilon_{kl}^{el} = \frac{1}{2}\Bigg[& \left(\frac{\partial C_{11}}{\partial\phi}(\varepsilon_{11}-\varepsilon_{11}^{g})+\frac{\partial C_{12}}{\partial\phi}(\varepsilon_{22}-\varepsilon_{22}^{g})\right.\\ & \left.+\frac{\partial C_{12}}{\partial\phi}\varepsilon_{33}\right)(\varepsilon_{11}-\varepsilon_{11}^{g})\\ & +\left(\frac{\partial C_{12}}{\partial\phi}(\varepsilon_{11}-\varepsilon_{11}^{g})+\frac{\partial C_{11}}{\partial\phi}(\varepsilon_{22}-\varepsilon_{22}^{g})\right.\\ & \left.+\frac{\partial C_{12}}{\partial\phi}\varepsilon_{33}\right)(\varepsilon_{22}-\varepsilon_{22}^{g})\\ & +\left(\frac{\partial C_{12}}{\partial\phi}(\varepsilon_{11}-\varepsilon_{11}^{g})+\frac{\partial C_{12}}{\partial\phi}(\varepsilon_{22}-\varepsilon_{22}^{g})\right.\\ & \left.+\frac{\partial C_{11}}{\partial\phi}\varepsilon_{33}\right)\varepsilon_{33}\\ & +4\varepsilon_{23}\varepsilon_{23}\frac{\partial C_{66}}{\partial\phi}+4\varepsilon_{13}\varepsilon_{13}\frac{\partial C_{66}}{\partial\phi}+4\varepsilon_{12}\varepsilon_{12}\frac{\partial C_{66}}{\partial\phi}\Bigg]\end{aligned} \tag{A.6}$$

$$\begin{aligned}\frac{\partial\varepsilon_{ij}^{el}}{\partial\phi}C_{ijkl}\varepsilon_{kl}^{el} = & \quad [C_{11}(\varepsilon_{11}-\varepsilon_{11}^{g})+C_{12}(\varepsilon_{22}-\varepsilon_{22}^{g})+C_{13}\varepsilon_{33}]\\ & \times\left(\frac{\partial\varepsilon_{11}}{\partial\phi}-\frac{\partial\varepsilon_{11}^{g}}{\partial\phi}\right)\\ & +[C_{12}(\varepsilon_{11}-\varepsilon_{11}^{g})+C_{11}(\varepsilon_{22}-\varepsilon_{22}^{g})+C_{23}\varepsilon_{33}]\left(\frac{\partial\varepsilon_{22}}{\partial\phi}-\frac{\partial\varepsilon_{22}^{g}}{\partial\phi}\right)\\ & +[C_{13}(\varepsilon_{11}-\varepsilon_{11}^{g})+C_{23}(\varepsilon_{22}-\varepsilon_{22}^{g})+C_{11}\varepsilon_{33}]\frac{\partial\varepsilon_{33}}{\partial\phi}\\ & +\left(4\varepsilon_{23}\frac{\partial\varepsilon_{23}}{\partial\phi}C_{66}+4\varepsilon_{13}\frac{\partial\varepsilon_{13}}{\partial\phi}C_{66}+4\varepsilon_{12}\frac{\partial\varepsilon_{12}}{\partial\phi}C_{66}\right)\end{aligned} \tag{A.7}$$

Finally, the governing equation of ϕ can be expressed as:

$$\begin{aligned}\dot{\phi} = & -L_{\phi}\Bigg(\frac{1}{2}\left[-i_{MO}\frac{\mathrm{d}p}{\mathrm{d}\phi}k_{M}\left(c-c_{M}\right)^{2}+\frac{\mathrm{d}p}{\mathrm{d}\phi}k_{O}\left(c-c_{O}\right)^{2}\right.\\ & \left.-i_{OP}\frac{\mathrm{d}p}{\mathrm{d}\phi}k_{P}\left(c-c_{P}\right)^{2}\right]+(i_{MO}W_{MO}+i_{OP}W_{OP})\frac{\mathrm{d}g}{\mathrm{d}\phi}\\ & -(i_{MO}\kappa_{MO}+i_{OP}\kappa_{OP})\nabla^{2}\phi+\frac{1}{2}\varepsilon_{ij}^{el}\frac{\partial C_{ijkl}}{\partial\phi}\varepsilon_{kl}^{el}+\frac{\partial\varepsilon_{ij}^{el}}{\partial\phi}C_{ijkl}\varepsilon_{kl}^{el}\Bigg)\\ & -L_{r}^{MO}\frac{\mathrm{d}p}{\mathrm{d}\phi}(c-c_{eq}^{MO})i_{MO}-L_{r}^{OP}\frac{\mathrm{d}p}{\mathrm{d}\phi}(c-c_{eq}^{OP})i_{OP}\end{aligned} \tag{A.8}$$

The Cahn–Hilliard equation (17) is expressed as a function of the derivative of the Gibbs free energy with respect to c. This term can be developed as following:

$$\frac{\delta G}{\delta c} = \frac{\partial f_{chem}^{Ni}}{\partial c} \tag{A.9}$$

$$\begin{aligned}\frac{\partial f_{chem}^{Ni}}{\partial c} = & \; i_{MO}(1-p(\phi))k_{M}\left(c-c_{M}\right)\\ & +(p(\phi))k_{O}\left(c-c_{O}\right)+i_{OP}(1-p(\phi))k_{P}\left(c-c_{P}\right)\end{aligned} \tag{A.10}$$

The developed form of the Cahn–Hilliard equation is:

$$\begin{aligned}\dot{c} = & \; \nabla\cdot\Big[M_{c}\nabla\Big(i_{MO}(1-p(\phi))k_{M}\left(c-c_{M}\right)+(p(\phi))k_{O}\left(c-c_{O}\right)\\ & +i_{OP}(1-p(\phi))k_{P}\left(c-c_{P}\right)\Big)\Big]-i_{OP}\frac{\mathrm{d}\phi}{\mathrm{d}t}\frac{1}{\eta}\end{aligned} \tag{A.11}$$

Appendix B. Supplementary data

Supplementary material related to this article can be found online at https://doi.org/10.1016/j.actamat.2026.122665.

References

[1] S. Mahmoudinezhad, M. Sadi, H. Ghiasirad, A. Arabkoohsar, A comprehensive review on the current technologies and recent developments in high-temperature heat exchangers, Renew. Sustain. Energy Rev. 183 (2023) 113467, http://dx.doi.org/10.1016/j.rser.2023.113467.

[2] M. Sarafraz, M.R. Safaei, M. Goodarzi, M. Arjomandi, Reforming of methanol with steam in a micro-reactor with cu–SiO2 porous catalyst, Int. J. Hydrog. Energy 44 (36) (2019) 19628–19639, http://dx.doi.org/10.1016/j.ijhydene.2019.05.215.

[3] S. Aruna, M. Muthuraman, K. Patil, Synthesis and properties of Ni-YSZ cermet: Anode material for solid oxide fuel cells, Solid State Ion. 111 (1–2) (1998) 45–51, http://dx.doi.org/10.1016/s0167-2738(98)00187-8.

[4] F. Yang, L. Zhang, J. Lin, Y. Liang, Y. He, S. Shang, Z.-K. Liu, Pore structure and gas permeability of high Nb-containing TiAl porous alloys by elemental powder metallurgy for microfiltration application, Intermetallics 33 (2013) 2–7, http://dx.doi.org/10.1016/j.intermet.2012.07.022.

[5] D. Hotza, M. Di Luccio, M. Wilhelm, Y. Iwamoto, S. Bernard, J.C. Diniz da Costa, Silicon carbide filters and porous membranes: A review of processing, properties, performance and application, J. Membr. Sci. 610 (2020) 118193, http://dx.doi.org/10.1016/j.memsci.2020.118193.

[6] P. Mechnich, M. Welter, Porous oxide ceramic matrix composites – properties, manufacturing, and applications, in: D. Brabazon (Ed.), Encyclopedia of Materials: Composites, Elsevier, Oxford, 2021, pp. 48–54, http://dx.doi.org/10.1016/B978-0-12-819724-0.00073-2.

[7] Q. Pang, G. Wu, Z. Xiu, L. Jiang, D. Sun, Microstructure, oxidation resistance and high-temperature strength of a new class of 3D open-cell nickel-based foams, Mater. Charact. 70 (2012) 125–136, http://dx.doi.org/10.1016/j.matchar.2012.05.010.

[8] W. Jiang, X. Ma, D. Zhang, Z. Li, P. Fu, Highly efficient catalysts for hydrogen generation through methanol steam reforming: A critical analysis of modification strategies, deactivation, mechanisms and kinetics, J. Ind. Eng. Chem. 130 (2024) 54–72, http://dx.doi.org/10.1016/j.jiec.2023.09.043.

[9] W. Gui, Y. Qu, Y. Liang, Y. Wang, H. Zhang, B. Luan, J. Lin, High efficiency hierarchical porous composite microfiltration membrane for high-temperature particulate matter capturing, Npj Mater. Degrad. 5 (1) (2021) http://dx.doi.org/10.1038/s41529-020-00147-0.

[10] H.F. López, Influence of porosity on the high temperature oxidation of a SiC-reinforced Si3N4 ceramic composite, J. Mater. Sci. 35 (23) (2000) 5995–6004, http://dx.doi.org/10.1023/a:1026746927762.

[11] A. Hauch, R. Küngas, P. Blennow, A.B. Hansen, J.B. Hansen, B.V. Mathiesen, M.B. Mogensen, Recent advances in solid oxide cell technology for electrolysis, Science 370 (6513) (2020) eaba6118, http://dx.doi.org/10.1126/science.aba6118, arXiv: https://www.science.org/doi/pdf/10.1126/science.aba6118.

[12] S.J. McPhail, S. Frangini, J. Laurencin, E. Effori, A. Abaza, A.K. Padinjarethil, A. Hagen, A. Léon, A. Brisse, D. Vladikova, B. Burdin, F.R. Bianchi, B. Bosio, P. Piccardo, R. Spotorno, H. Uchida, P. Polverino, E.A. Adinolfi, F. Postiglione, J.-H. Lee, H. Moussaoui, J. Van herle, Addressing planar solid oxide cell degradation mechanisms: A critical review of selected components, Electrochem. Sci. Adv. 2 (5) (2021) http://dx.doi.org/10.1002/elsa.202100024.

[13] N.B. Pilling, R.E. Bedworth, The oxidation of metals at high temperatures, J. Inst. Met. (1923) 529–591.

[14] M. Schütze, Protective Oxide Scales and their Breakdown, Wiley, Chichester, 1997.

[15] R. Peraldi, D. Monceau, S. Jean, B. Pieraggi, High temperature oxidation of high purity nickel: Oxide scale morphology and growth kinetics, Mater. High Temp. 20 (4) (2003) 649–655, http://dx.doi.org/10.1179/mht.2003.073.

[16] S. De Angelis, P.S. Jørgensen, V. Esposito, E.H.R. Tsai, M. Holler, K. Kreka, E. Abdellahi, J.R. Bowen, Ex-situ tracking solid oxide cell electrode microstructural evolution in a redox cycle by high resolution ptychographic nanotomography, J. Power Sources 360 (2017) 520–527, http://dx.doi.org/10.1016/j.jpowsour.2017.06.035.

[17] J. Laurencin, G. Delette, O. Sicardy, S. Rosini, F. Lefebvre-Joud, Impact of 'redox' cycles on performances of solid oxide fuel cells: Case of the electrolyte supported cells, J. Power Sources 195 (9) (2010) 2747–2753, http://dx.doi.org/10.1016/j.jpowsour.2009.10.099.

[18] A. Nakajo, A.M. Kiss, A.P. Cocco, W.M. Harris, M.B. DeGostin, F. Greco, G.J. Nelson, A.A. Peracchio, B.N. Cassenti, A. Deriy, S. Wang, Y. Chen-Wiegart, J. Wang, J. Van herle, W.K.S. Chiu, Characterization of cracks and their effects on the effective transport pathways in Ni-YSZ anodes after reoxidation using X-Ray nanotomography, ECS Trans. 68 (1) (2015) 1069, http://dx.doi.org/10.1149/06801.1069ecst.

[19] D. Sarantaridis, R. Rudkin, A. Atkinson, Oxidation failure modes of anode-supported solid oxide fuel cells, J. Power Sources 180 (2) (2008) 704–710, http://dx.doi.org/10.1016/j.jpowsour.2008.03.011.

[20] A. Faes, A. Nakajo, A. Hessler-Wyser, D. Dubois, A. Brisse, S. Modena, J. Van herle, Redox study of anode-supported solid oxide fuel cell, J. Power Sources 193 (1) (2009) 55–64, http://dx.doi.org/10.1016/j.jpowsour.2008.12.118, Scientific Advances in Fuel Cell Systems.

[21] A. Atkinson, R.I. Taylor, P.D. Goode, Transport processes in the oxidation of Ni studied using tracers in growing NiO scales, Oxid. Met. 13 (6) (1979) 519–543, http://dx.doi.org/10.1007/bf00812776.

[22] A. Atkinson, R.I. Taylor, The diffusion of 63Ni along grain boundaries in nickel oxide, Phil. Mag. A 43 (4) (1981) 979–998, http://dx.doi.org/10.1080/01418618108239506.

[23] A. Atkinson, R.I. Taylor, A.E. Hughes, A quantitative demonstration of the grain boundary diffusion mechanism for the oxidation of metals, Phil. Mag. A 45 (5) (1982) 823–833, http://dx.doi.org/10.1080/01418618208239905.

[24] A. Atkinson, D.W. Smart, Transport of nickel and oxygen during the oxidation of nickel and dilute nickel/chromium alloy, J. Electrochem. Soc. 135 (11) (1988) 2886–2893, http://dx.doi.org/10.1149/1.2095454.

[25] R. Haugsrud, On the high-temperature oxidation of nickel, Corros. Sci. 45 (1) (2003) 211–235, http://dx.doi.org/10.1016/s0010-938x(02)00085-9.

[26] C. Wagner, Theoretical analysis of the diffusion processes determining the oxidation rate of alloys, J. Electrochem. Soc. 99 (10) (1952) 369, http://dx.doi.org/10.1149/1.2779605.

[27] K. Kim, Q.C. Sherman, L.K. Aagesen, P.W. Voorhees, Phase-field model of oxidation: Kinetics, Phys. Rev. E 101 (2) (2020) http://dx.doi.org/10.1103/physreve.101.022802.

[28] A. Atkinson, Transport processes during the growth of oxide films at elevated temperature, Rev. Modern Phys. 57 (2) (1985) 437–470, http://dx.doi.org/10.1103/revmodphys.57.437.

[29] R. Peraldi, D. Monceau, B. Pieraggi, Correlations between growth kinetics and microstructure for scales formed by high-temperature oxidation of pure nickel. I. Morphologies and microstructures, Oxid. Met. 58 (3/4) (2002) 249–273, http://dx.doi.org/10.1023/a:1020170320020.

[30] H.E. Evans, Cavity formation and metallurgical changes induced by growth of oxide scale, Mater. Sci. Technol. 4 (12) (1988) 1089–1098, http://dx.doi.org/10.1179/mst.1988.4.12.1089.

[31] D. Sarantaridis, R.J. Chater, A. Atkinson, Changes in physical and mechanical properties of SOFC Ni–YSZ composites caused by redox cycling, J. Electrochem. Soc. 155 (5) (2008) B467, http://dx.doi.org/10.1149/1.2883731.

[32] F.H. Stott, A. Atkinson, The modelling of growth stresses during high-temperature oxidation, Mater. High Temp. 12 (2–3) (1994) 195–207, http://dx.doi.org/10.1080/09603409.1994.11689487.

[33] B. Pieraggi, R. Rapp, Stress generation and vacancy annihilation during scale growth limited by cation-vacancy diffusion, Acta Metall. 36 (5) (1988) 1281–1289, http://dx.doi.org/10.1016/0001-6160(88)90280-5.

[34] B. Pieraggi, R.A. Rapp, J.P. Hirth, Role of interface structure and interfacial defects in oxide scale growth, Oxid. Met. 44 (1–2) (1995) 63–79, http://dx.doi.org/10.1007/bf01046723.

[35] H. Kyung, C. Kim, Microstructural evolution of duplex grain structure and interpretation of the mechanism for NiO scales grown on pure Ni- and Cr-doped substrates during high temperature oxidation, Mater. Sci. Eng.: B 76 (3) (2000) 173–183, http://dx.doi.org/10.1016/s0921-5107(00)00435-9.

[36] A. Heuer, T. Nakagawa, M. Azar, D. Hovis, J. Smialek, B. Gleeson, N. Hine, H. Guhl, H.-S. Lee, P. Tangney, W. Foulkes, M. Finnis, On the growth of Al2O3 scales, Acta Mater. 61 (18) (2013) 6670–6683, http://dx.doi.org/10.1016/j.actamat.2013.07.024.

[37] Q. Jeangros, T. Hansen, J. Wagner, R. Dunin-Borkowski, C. Hébert, J. Van herle, A. Hessler-Wyser, Oxidation mechanism of nickel particles studied in an environmental transmission electron microscope, Acta Mater. 67 (2014) 362–372, http://dx.doi.org/10.1016/j.actamat.2013.12.035.

[38] D. Clarke, The lateral growth strain accompanying the formation of a thermally grown oxide, Acta Mater. 51 (5) (2003) 1393–1407, http://dx.doi.org/10.1016/s1359-6454(02)00532-3.

[39] G.C. Wood, J. Stringer, The adhesion of growing oxide scales to the substrate, J. Phys. IV 03 (C9) (1993) C9–65–C9–74, http://dx.doi.org/10.1051/jp4:1993904.

[40] J. Robertson, M.I. Manning, Limits to adherence of oxide scales, Mater. Sci. Technol. 6 (1) (1990) 81–92, http://dx.doi.org/10.1179/mst.1990.6.1.81.

[41] R. Peraldi, D. Monceau, B. Pieraggi, Correlations between growth kinetics and microstructure for scales formed by high-temperature oxidation of pure nickel. II. Growth kinetics, Oxid. Met. 58 (3/4) (2002) 275–295, http://dx.doi.org/10.1023/a:1020102604090.

[42] F.N. Rhines, J.S. Wolf, The role of oxide microstructure and growth stresses in the high-temperature scaling of nickel, Met. Trans. 1 (6) (1970) 1701–1710, http://dx.doi.org/10.1007/bf02642020.

[43] A.-M. Huntz, B. Pieraggi, Oxydation des Matériaux Métalliques: Comportement à Haute Température, Hermes-Lavoisier, 2003.

[44] D.J. Srolovitz, T.A. Ramanarayanan, An elastic analysis of growth stresses during oxidation, Oxid. Met. 22 (3–4) (1984) 133–146, http://dx.doi.org/10.1007/bf00656901.

[45] Z. Peide, F.H. Stott, R.P.M. Procter, W.A. Grant, The early stages of oxidation of ion-implanted nickel at high temperature, Oxid. Met. 16 (5–6) (1981) 409–426, http://dx.doi.org/10.1007/bf00611353.

[46] J. Malzbender, E. Wessel, R. Steinbrech, Reduction and re-oxidation of anodes for solid oxide fuel cells, Solid State Ion. 176 (29–30) (2005) 2201–2203, http://dx.doi.org/10.1016/j.ssi.2005.06.014.

[47] Q. Jeangros, A. Faes, J. Wagner, T. Hansen, U. Aschauer, J. Van herle, A. Hessler-Wyser, R. Dunin-Borkowski, In situ redox cycle of a nickel–YSZ fuel cell anode in an environmental transmission electron microscope, Acta Mater. 58 (14) (2010) 4578–4589, http://dx.doi.org/10.1016/j.actamat.2010.04.019.

[48] M. Ettler, H. Timmermann, J. Malzbender, A. Weber, N. Menzler, Durability of Ni anodes during reoxidation cycles, J. Power Sources 195 (17) (2010) 5452–5467, http://dx.doi.org/10.1016/j.jpowsour.2010.03.049.

[49] J. Laurencin, V. Roche, C. Jaboutian, I. Kieffer, J. Mougin, M. Steil, Ni-8YSZ cermet re-oxidation of anode supported solid oxide fuel cell: From kinetics measurements to mechanical damage prediction, Int. J. Hydrog. Energy 37 (17) (2012) 12557–12573, http://dx.doi.org/10.1016/j.ijhydene.2012.06.019.

[50] J.W. Cahn, J.E. Hilliard, Free energy of a nonuniform system. I. Interfacial free energy, J. Chem. Phys. 28 (2) (1958) 258–267, http://dx.doi.org/10.1063/1.1744102.

[51] S. Allen, J. Cahn, Ground state structures in ordered binary alloys with second neighbor interactions, Acta Metall. 20 (3) (1972) 423–433, http://dx.doi.org/10.1016/0001-6160(72)90037-5.

[52] L.-Q. Chen, Y. Zhao, From classical thermodynamics to phase-field method, Prog. Mater. Sci. 124 (2022) 100868, http://dx.doi.org/10.1016/j.pmatsci.2021.100868.

[53] R. Wang, Y. Ji, T.-L. Cheng, F. Xue, L.-Q. Chen, Y.-H. Wen, Phase-field modeling of alloy oxidation at high temperatures, Acta Mater. 248 (2023) 118776, http://dx.doi.org/10.1016/j.actamat.2023.118776.

[54] Y. Zhao, S. Ai, D. Fang, Elasto-plastic phase field modelling of oxidation of zirconium alloys, Int. J. Solids Struct. 134 (2018) 30–42, http://dx.doi.org/10.1016/j.ijsolstr.2017.10.033.

[55] K. Ammar, B. Appolaire, G. Cailletaud, F. Feyel, S. Forest, Finite element formulation of a phase field model based on the concept of generalized stresses, Comput. Mater. Sci. 45 (3) (2009) 800–805, http://dx.doi.org/10.1016/j.commatsci.2008.09.015.

[56] Q.C. Sherman, P.W. Voorhees, Phase-field model of oxidation: Equilibrium, Phys. Rev. E 95 (3) (2017) http://dx.doi.org/10.1103/physreve.95.032801.

[57] C. Lin, H. Ruan, Phase-field modeling of scale roughening induced by outward growing oxide, Materialia 5 (2019) 100255, http://dx.doi.org/10.1016/j.mtla.2019.100255.

[58] M. Asle Zaeem, H. El Kadiri, An elastic phase field model for thermal oxidation of metals: Application to zirconia, Comput. Mater. Sci. 89 (2014) 122–129, http://dx.doi.org/10.1016/j.commatsci.2014.03.042.

[59] M. Johnson, Phase Field Modelling of Nickel Oxidation (Ph.D. thesis), University of Birmingham, 2022.

[60] Z. Jiao, N. Shikazono, Simulation of the reduction process of solid oxide fuel cell composite anode based on phase field method, J. Power Sources 305 (2016) 10–16, http://dx.doi.org/10.1016/j.jpowsour.2015.11.061.

[61] F. Abdeljawad, G.J. Nelson, W.K.S. Chiu, M. Haataja, Redox instability, mechanical deformation, and heterogeneous damage accumulation in solid oxide fuel cell anodes, J. Appl. Phys. 112 (3) (2012) http://dx.doi.org/10.1063/1.4745038.

[62] A. Abaza, Fracture of Porous Ceramics : Application to the Mechanical Degradation of Solid Oxide Cells During Redox Cycling (Ph.D. thesis), Université Grenoble Alpes, 2022.

[63] F. Xue, Y. Lei, T.-L. Cheng, W.K. Epting, G. Hackett, H. Abernathy, Y.-H. Wen, Phase-field modeling of crack growth and mitigation in solid oxide cells, Int. J. Hydrog. Energy 48 (26) (2023) 9845–9860, http://dx.doi.org/10.1016/j.ijhydene.2022.12.042.

[64] E. Da Rosa Silva, G. Sassone, M. Prioux, M. Hubert, B. Morel, J. Laurencin, A multiscale model validated on local current measurements for understanding the solid oxide cells performances, J. Power Sources 556 (2023) 232499, http://dx.doi.org/10.1016/j.jpowsour.2022.232499.

[65] S. van der Walt, J.L. Schönberger, J. Nunez-Iglesias, F. Boulogne, J.D. Warner, N. Yager, E. Gouillart, T. Yu, Scikit-image: Image processing in Python, PeerJ 2 (2014) e453, http://dx.doi.org/10.7717/peerj.453.

[66] K. Dia, T. David, L. Guetaz, Z. Saghi, G. Daniel, Enhanced phase segmentation of scanning electron microscopy images using U-net with energy dispersive X-ray spectroscopy-guided labelling, Mater. Des. 260 (2025) 115200, http://dx.doi.org/10.1016/j.matdes.2025.115200.

[67] J. Laurencin, G. Delette, B. Morel, F. Lefebvre-Joud, M. Dupeux, Solid oxide fuel cells damage mechanisms due to Ni-YSZ re-oxidation: Case of the anode supported cell, J. Power Sources 192 (2) (2009) 344–352, http://dx.doi.org/10.1016/j.jpowsour.2009.02.089.

[68] T.-L. Cheng, Y. Lei, Y. Chen, Y. Fan, H. Abernathy, X. Song, Y.-H. Wen, Oxidation of nickel in solid oxide cells during electrochemical operation: Experimental evidence, theoretical analysis, and an alternative hypothesis on the nickel migration, J. Power Sources 569 (2023) 232991, http://dx.doi.org/10.1016/j.jpowsour.2023.232991.

[69] S.-L. Wang, R. Sekerka, A. Wheeler, B. Murray, S. Coriell, R. Braun, G. McFadden, Thermodynamically-consistent phase-field models for solidification, Phys. D 69 (1–2) (1993) 189–200, http://dx.doi.org/10.1016/0167-2789(93)90189-8.

[70] S.G. Kim, W.T. Kim, T. Suzuki, Phase-field model for binary alloys, Phys. Rev. E 60 (6) (1999) 7186–7197, http://dx.doi.org/10.1103/PhysRevE.60.7186.

[71] Z. Xiao, X.-M. Bai, First-principle studies of oxidation effects on grain boundary strength in nickel, Materialia 28 (2023) 101745, http://dx.doi.org/10.1016/j.mtla.2023.101745.

[72] I. Leonov, S. Biermann, Electronic correlations at paramagnetic (001) and (110) NiO surfaces: Charge-transfer and Mott-Hubbard-type gaps at the surface and subsurface of (110) NiO, Phys. Rev. B 103 (16) (2021) http://dx.doi.org/10.1103/physrevb.103.165108.

[73] T.-L. Cheng, Y.-H. Wen, J.A. Hawk, Diffuse-interface modeling and multiscale-relay simulation of metal oxidation kinetics—With revisit on Wagner's theory, J. Phys. Chem. C 118 (2) (2014) 1269–1284, http://dx.doi.org/10.1021/jp409811e.

[74] Y. Unutulmazsoy, R. Merkle, D. Fischer, J. Mannhart, J. Maier, The oxidation kinetics of thin nickel films between 250 and 500 °C, Phys. Chem. Chem. Phys. 19 (13) (2017) 9045–9052, http://dx.doi.org/10.1039/c7cp00476a.

[75] T.-L. Cheng, F. Xue, Y. Lei, R.P. Oleksak, Ö.N. Doğan, Y.-H. Wen, Phase-field modeling of thermally-grown oxide and damage evolution in environmental barrier coatings, Acta Mater. 284 (2025) 120571, http://dx.doi.org/10.1016/j.actamat.2024.120571.

[76] J. Villanova, O. Sicardy, R. Fortunier, J.S. Micha, P. Bleuet, X-Ray diffraction determination of macro and micro stresses in SOFC electrolyte and evolution with redox cycling of the anode, Mater. Sci. Forum 681 (2011) 25–30, http://dx.doi.org/10.4028/www.scientific.net/msf.681.25.

[77] J. Villanova, Détermination des Contraintes Résiduelles dans les Matériaux Céramiques Pour SOFC : Mesures Multi-Échelles et Influence des Cycles D'oxydo-Réduction. Mécanique (Ph.D. thesis), Ecole Nationale Supérieure des Mines de Saint-Etienne, 2010.

[78] B. Panicaud, Contraintes "De Croissance" et Cinétiques D'oxydation dans des Couches D'oxydes Thermiques de fer et de Nickel ; Etude In-Situ Par Diffraction des Rayons X et Modélisation (theses), Université de La Rochelle, 2004.

[79] R. Krishnamurthy, D. Srolovitz, Stress distributions in growing polycrystalline oxide films, Acta Mater. 52 (13) (2004) 3761–3780, http://dx.doi.org/10.1016/j.actamat.2004.04.036.

[80] H. Evans, The role of oxide grain boundaries in the development of growth stresses during oxidation, Corros. Sci. 23 (5) (1983) 495–506, http://dx.doi.org/10.1016/0010-938x(83)90099-9.

[81] H. Moussaoui, J. Laurencin, Y. Gavet, G. Delette, M. Hubert, P. Cloetens, T. Le Bihan, J. Debayle, Stochastic geometrical modeling of solid oxide cells electrodes validated on 3D reconstructions, Comput. Mater. Sci. 143 (2018) 262–276, http://dx.doi.org/10.1016/j.commatsci.2017.11.015.

[82] M. Ouyang, A. Bertei, S.J. Cooper, Y. Wu, P. Boldrin, X. Liu, M. Kishimoto, H. Wang, M. Naylor Marlow, J. Chen, X. Chen, Y. Xia, B. Wu, N.P. Brandon, Model-guided design of a high performance and durability Ni nanofiber/ceria matrix solid oxide fuel cell electrode, J. Energy Chem. 56 (2021) 98–112, http://dx.doi.org/10.1016/j.jechem.2020.07.026.

[83] Y. Chen, S. Chen, G. Hackett, H. Finklea, X. Song, K. Gerdes, Microstructural and chemical evolution near anode triple phase boundary in Ni/YSZ solid oxide fuel cells, Solid State Ion. 204–205 (2011) 87–90, http://dx.doi.org/10.1016/j.ssi.2011.10.005.

[84] T. Sasaki, K. Matsunaga, H. Ohta, H. Hosono, T. Yamamoto, Y. Ikuhara, Atomic and electronic structures of Ni/YSZ(111) interface, Mater. Trans. 45 (7) (2004) 2137–2143, http://dx.doi.org/10.2320/matertrans.45.2137.

[85] W.M. Haynes, CRC Handbook of Chemistry and Physics, ninety-fifth ed., CRC Press, 2014, http://dx.doi.org/10.1201/b17118.

[86] K. Maier, H. Mehrer, E. Lessmann, W. Schüle, Self-diffusion in nickel at low temperatures, Phys. Status Solidi (B) 78 (2) (1976) 689–698, http://dx.doi.org/10.1002/pssb.2220780230.

[87] O. Hubert, X. Milhet, P. Gadaud, M. Tatat, P.-O. Renault, C. Coupeau, Modeling of Young's modulus variations with temperature of Ni and oxidized Ni using a magneto-mechanical approach, Mater. Sci. Eng.: A 633 (2015) 76–91, http://dx.doi.org/10.1016/j.msea.2015.03.014.

[88] I.A. Menzies, K.N. Strafford, Observations on the mechanical properties of nickel oxide scales, J. Mater. Sci. 2 (4) (1967) 358–364, http://dx.doi.org/10.1007/bf00572420.

[89] Y.Y. Liu, K. Natesan, The adherence of nickel oxide on nickel during high-temperature oxidation, MRS Proc. 119 (1988) http://dx.doi.org/10.1557/proc-119-213.

[90] D. Monceau, R. Peraldi, B. Pieraggi, Diffusion and high-temperature oxidation of nickel, Defect Diffus. Forum 194–199 (2001) 1675–1682, http://dx.doi.org/10.4028/www.scientific.net/ddf.194-199.1675.

[91] F. Xue, T.-L. Cheng, Y.-H. Wen, Stress analysis of the steam-side oxide of boiler tubes: Contributions from thermal strain, interface roughness, creep, and oxide growth, Oxid. Met. 93 (5–6) (2020) 515–543, http://dx.doi.org/10.1007/s11085-020-09969-4.

[92] J. Zhang, J. Wang, Y. Tang, Z. Qu, X. Feng, A curvature-dependent chemo-mechanical coupling model for two-dimensional oxidation on the curved surface, Int. J. Solids Struct. 279 (2023) 112363, http://dx.doi.org/10.1016/j.ijsolstr.2023.112363.

[93] D. Leguillon, Strength or toughness? A criterion for crack onset at a notch, Eur. J. Mech. A Solids 21 (1) (2002) 61–72, http://dx.doi.org/10.1016/s0997-7538(01)01184-6.

[94] A. Abaza, J. Laurencin, A. Nakajo, S. Meille, J. Debayle, D. Leguillon, Prediction of crack nucleation and propagation in porous ceramics using the phase-field approach, Theor. Appl. Fract. Mech. 119 (2022) 103349, http://dx.doi.org/10.1016/j.tafmec.2022.103349.

[95] M. Hubert, J. Laurencin, P. Cloetens, J. Mougin, D. Ferreira Sanchez, S. Pylypko, M. Morales, A. Morata, B. Morel, D. Montinaro, E. Siebert, F. Lefebvre-Joud, Solid oxide cell degradation operated in fuel cell and electrolysis modes: A comparative study on Ni agglomeration and LSCF destabilization, ECS Trans. 78 (1) (2017) 3167–3177, http://dx.doi.org/10.1149/07801.3167ecst.

[96] A. Trivino-Pelaez, D. Cademartori, M. Hubert, L. Rorato, M. Prioux, J. Laurencin, Modelling the impact of Ni migration and coarsening on the Ni-YSZ electrodes performances based on three-dimensional microstructures, Electrochim. Acta 520 (2025) 145791, http://dx.doi.org/10.1016/j.electacta.2025.145791.

[97] D. Cademartori, M. Hubert, E. Bonnet, J.M. Bassat, J. Laurencin, Engineering nanostructured electrodes for solid oxide cells (SOCs) via microstructural and electrochemical modelling, Int. J. Hydrog. Energy 98 (2025) 1396–1414, http://dx.doi.org/10.1016/j.ijhydene.2024.11.484.

[98] M. Avrami, Kinetics of phase change. I general theory, J. Chem. Phys. 7 (12) (1939) 1103–1112, http://dx.doi.org/10.1063/1.1750380.

[99] M. Prioux, E. Da Rosa Silva, M. Hubert, J. Vulliet, J. Debayle, P. Cloetens, J. Laurencin, Numerical microstructural optimization for the hydrogen electrode of solid oxide cells, Fuel Cells 23 (6) (2023) 408–419, http://dx.doi.org/10.1002/fuce.202300029.